Institut für Theoretische Physik
Universität zu köln

Strongly correlated critical chiral paramagnets

Master thesis by
Laura Köhler

First Examiner: Prof. Dr. Achim Rosch
Second Examiner: PD Dr. Markus Garst

November 2015

Abstract

Chiral paramagnet are materials which are characterised by a lack of inversion symmetry. Due to strong correlations in chiral paramagnets, a new region arises in the phase diagram in addition to the magnetically ordered phases, namely the fluctuation disordered (FD) regime [1, 2, 3]. Resonance experiments in the FD regime show a shift to higher frequencies compared to the paramagnetic phase [4].

We address the fluctuations by applying perturbation theory up to second order and calculating the self-energy in this approximation. We use the self-energy to renormalise the susceptibility and qualitatively compare the position of the maximum as a function of magnetic field with the experiments. We show that including the self-energy shifts the maximum of the imaginary part of the susceptibility to higher frequencies for small magnetic fields. This is in accordance with the experimental observations. For higher fields, however, we are not able to reproduce the experimental behaviour.

Furthermore, we investigate the processes taking place as well as the type of the fluctuations, i. e. if they have a helical or even a skyrmionic nature. We will show that the fluctuations consist of three overlapping helices. Their pitch vectors build triangles. However, skyrmion type fluctuations appear not to be dominant. The dominant processes are those where two magnons are absorbed and one is emitted or vice versa, i. e. where two are emitted and one is absorbed.

Contents

Part I. Introduction

Since in 2009 skyrmions were measured for the first time in MnSi, great research activity started in the field of chiral magnets [5]. Skyrmions are topologically stable field configurations of the local magnetisation.

In chiral paramagnets such as MnSi, lattice structures occur which are not inversion invariant. This allows for an additional term in the free energy, which is only invariant under a combined rotation in spin space and real space, the Dzyaloshinskii-Moriya interaction [6, 7]. This term is of the form

$$D\vec{M} \cdot \left(\nabla \times \vec{M}\right).$$

The local magnetisation $\vec{M}$ is the order parameter of the theory. In contrast to the kinetic term, the one proportional to $\vec{M}^2$, this term favours a spin configuration with neighbouring spins being perpendicular to each other. This gives rise to different magnetic structures such as helices in the conical and helical phase or skyrmions in the skyrmionic phase [5, 2].

For high temperatures compared to the critical point at $T_c = 29\,\mathrm{K}$, the Dzyaloshinskii-Moriya interaction can be neglected. This is the case in the paramagnetic and the field polarised regime. However, when decreasing the temperature, it becomes more dominant.

In 2013 research groups from Munich and Cologne investigated the phase transitions in chiral paramagnets [1, 2, 3]. They found that, due to strong fluctuations, the critical temperature is suppressed and the phase transition between the paramagnetic phase and the conical or skyrmionic phase is driven to first order. This gives rise to a new regime between these two phases, the fluctuation disordered (FD) regime. In this thesis, we are interested in the fluctuation disordered regime.

At the Technische Universität in Munich Ioannis Stasinopoulos performed resonance experiments in the FD regime [4]. He observed a deviation from the Lamor frequency ω_{ferro} which is present in the paramagnetic regime. The experimentally observed maximum position in the FD regime is shifted to higher frequencies compared to the ferromagnetic resonance frequency [4].

The aim of this thesis is to explain theoretically the experimental behaviour observed in these resonance experiments. The width of the observed peaks increases with decreasing field. What we are thus looking for is not a singularity in the imaginary part of the susceptibility, in which case we would expect a sharp delta peak. We are looking for a broader maximum.

We ask the question, whether the strong fluctuations that occur in the FD regime, could give rise to this resonance behaviour. In the FD regime the Dzyaloshinskii-

Moriya interaction cannot be neglected anymore. Therefore, short range helical or even skyrmion type fluctuations can appear. They are not stable and they do not extend over the whole crystal. However, they can influence the behaviour in resonance experiments.

The excitation modes of skyrmions lie above the ferromagnetic resonance frequency. Therefore, skyrmions could well be responsible for the shift of the resonance to higher frequencies.

To describe chiral paramagnets, we use the Ginzburg-Landau theory with the Dzyaloshinskii-Moriya interaction term. The theory for chiral magnets will be introduced in Part II. In Part III we address the fluctuations by applying perturbation theory up to second order in the parameter u, which is the factor in front of the interaction term, i. e. the quartic term in the fields.

To calculate the resonances, we add dynamics to the model in a way similar to the one that yields the ferromagnetic resonances in the limit of a vanishing frequency and momentum. Meanwhile, we neglect any damping terms. This will be presented in section 3.

In section 4 we will take a closer look at the Green's function. We examine the spectrum for the static case without and with an external magnetic field and for the dynamical case.

We calculate the self-energy in section 5. The results are discussed in more detail in section 6. We use the calculated self-energy to renormalise the susceptibility in section 7. We focus on the imaginary part of the susceptibility since we are interested in the absorption. The maximum of this curve should be the frequency measured by the experimentalists.

We show that helices contribute to the self-energy. They always appear in groups of three and their pitch vectors build triangles. However, we do not observe any exceptional contribution from equilateral triangles lying in the equatorial plane. These would correspond to skyrmions. Skyrmion type fluctuations are therefore not the reason for the resonance shift.

In the imaginary part of the susceptibility we observe a deviation of the maximum from the Lamor frequency to higher frequencies for small external magnetic fields. To make the connection to the experiments, one needs to keep the perturbation parameter u in mind. It needs to be sufficiently small to stay in a regime where perturbation theory is valid. The experimental value of u given in [1] does not comply with that restriction. We can hence give a qualitative explanation of the experiments, yet we cannot reproduce quantitative results with this model.

For higher magnetic fields the calculated maximum position shifts to zero before approaching ω_{ferro} for high fields. These processes are neither experimentally nor physically plausible. This remains an open problem and requires further investigation. However, for high fields or small u the self-energy just broadens the delta peak at ω_{ferro} as expected in the paramagnetic phase.

Part II.
Theory of chiral paramagnets

This part introduces the basic theoretical concepts and the theory we use to describe critical chiral paramagnets.

For this whole thesis it is assumed that the external magnetic field points in z-direction.

1. Phase diagram

Figure 1 shows the phase diagram of bulk MnSi, which is a chiral paramagnet [2]. The phases depend on the temperature and the external magnetic field. It is investigated in [2], [5] and [1].

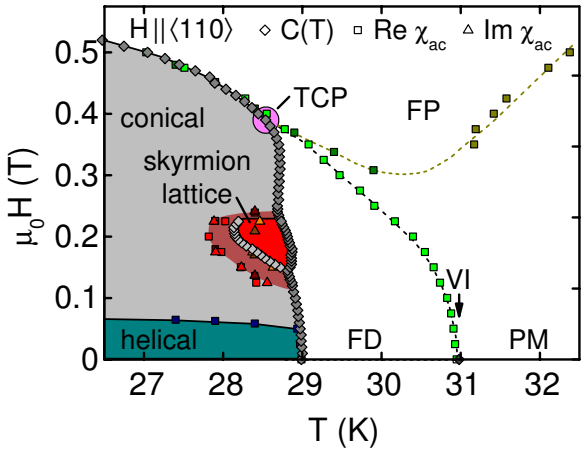

Figure 1: Phase diagram of MnSi [2]

For low temperatures $T \ll T_c$ the magnetisation forms a helical structure. At zero magnetic field, these helices lack a mean magnetisation (helical phase). Increasing the magnetic field, one passes a crossover into the conical phase. There the spins are twisted in the direction of the magnetic field, and, therefore, the helices do obtain a mean magnetisation. Said crossover, which separates the two regimes, depends on the crystalline direction, i. e. the anisotropies in the crystal, and the direction of the external magnetic field [8]. When increasing the magnetic field further, one finally arrives at a second order phase transition to the field polarised (FP) regime.

Following the mentioned second order phase transition, one arrives at the tricritical point (TCP) where the second order transition becomes first order due to fluctuations. In the fluctuation disordered regime (FD) there occur strong correlations which drive the transition to first order and lower the critical temperature of the

transition in comparison to mean-field theory (green dots). This regime can be described by the Brazovskii theory (cf. subsection 2.2). The mean-field line defines the crossover to the paramagnetic regime (PM).

For a certain range of magnetic field and temperature close to T_c there occurs another area in the phase diagram, namely the skyrmion lattice phase (red pocket). In this region a skyrmion lattice forms and remains stable.

1.1. Skyrmions

Skyrmions in solids were measured for the first time in 2009 by S. Mühlbauer [5]. This was the beginning of intense research in the field of skyrmions in the following years until today. However, Tony Skyrme originally introduced skyrmions in the context of high energy physics already in 1961 [9, 10].

A skyrmion is a field configuration which is smooth and topologically stable. Its winding number W is defined as

$$W = \int \frac{dx\,dy}{4\pi}\,\hat{\Omega}\cdot\left(\partial_x\hat{\Omega}\times\partial_y\hat{\Omega}\right), \tag{1.1}$$

with $\hat{\Omega} = \vec{M}/|\vec{M}|$ being the direction of the magnetisation, and $\vec{B}$ pointing in z-direction. It can either have the value 1 or -1. This means that it is impossible to smoothly change from one skyrmion (winding number ± 1) to no skyrmion (winding number 0). Thus, the skyrmion is topologically stable. The skyrmion has no winding at infinity. One can identify the skyrmion density with

$$\rho_{\text{skyrm}} = \frac{1}{4\pi}\,\hat{\Omega}\cdot\left(\partial_x\hat{\Omega}\times\partial_y\hat{\Omega}\right) \tag{1.2}$$

since this counts how many skyrmions are present when integrating over it [5, 11].

In the skyrmion phase the skyrmions build a two dimensional triangular lattice perpendicular to the magnetic field. A skyrmion can be described by a superposition of three helices where the pitch vectors build an equilateral triangle in the equatorial plane. This relation will become more obvious in subsection 1.2.

Figure 2 shows an image of a skyrmion and its projection on a sphere. Figure 2a shows a chiral skyrmion in real space. The arrows denote the local magnetisation. The external magnetic field points in z-direction, i. e. up. In the middle, the magnetisation points in opposite direction, namely down. When increasing the distance to the center, the magnetisation twists around until it points up. The left sphere, figure 2b, is the inverse stereographic projection of a Néel skyrmion, i. e. a non-chiral skyrmion. The center is thereby projected on the south pole and infinity on the north pole. This looks like a hedgehog. In this thesis we are considering chiral or Bloch skyrmions. The inverse stereographic projection of a chiral skyrmion is shown in figure 2c. Here, the hedgehog is combed in ϕ-direction (in standard spherical coordinates). Chiral skyrmions are stabilised by the Dzyaloshinskii-Moriya

interaction, which is represented by a term of the form $D\vec{M} \cdot (\nabla \times \vec{M})$ in the free energy [6, 7, 11].

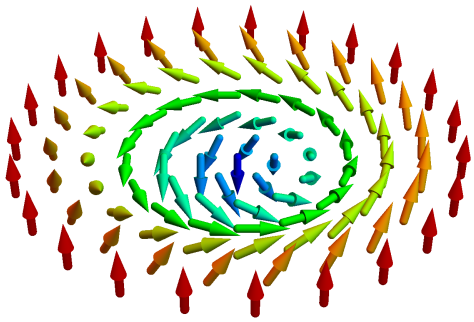

(a) Chiral skyrmion

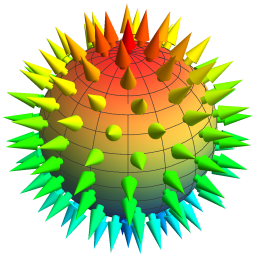

(b) Néel skyrmion

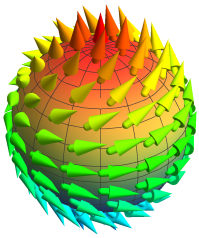

(c) Bloch skyrmion

Figure 2: (a) is a real space picture of a chiral skyrmion and (c) shows its projection on a sphere. (b) shows the inverse stereographic projection of a Néel skyrmion.

In the skyrmionic phase, there exist three excitation modes that can be excited by ferromagnetic resonance experiments. The skyrmions can rotate clockwise or anticlockwise in the clockwise respectively anticlockwise gyration mode. In addition, they can change in size in the breathing mode [12]. These modes are illustrated in figure 3.

In [12] the theoretical prediction for the excitation modes are given and compared to the experiments. In figure 4 one can see the resonance frequencies in the different phases of a typical chiral magnet as a function of the magnetic field. In the skyrmion phase (pink) one can observe the three modes described above. The ferromagnetic resonance frequency corresponds to the continuation of the straight line defined by the frequencies in the field polarised (FP) region. The anticlockwise gyration mode and the breathing mode are located at higher frequencies than a ferromagnetic resonance would be at the corresponding magnetic field.

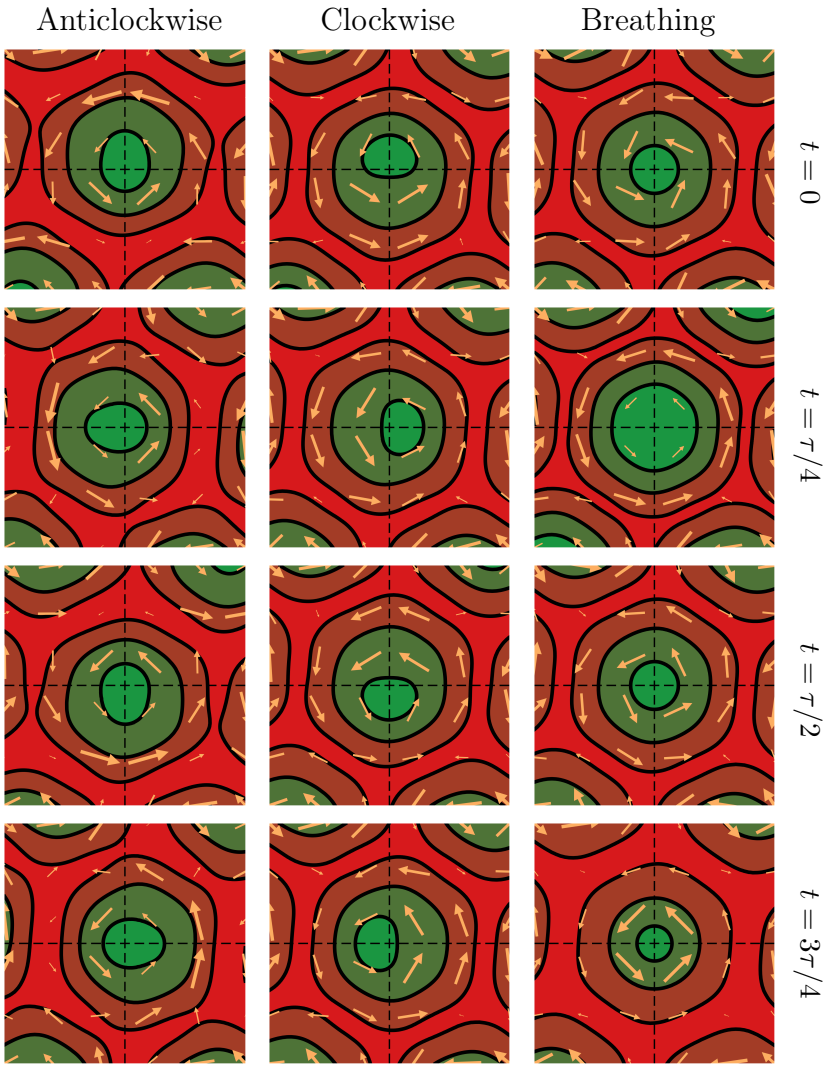

Figure 3: Skyrmionic excitation: the anticlockwise (left) and clockwise (middle) gyration modes and the breathing mode (right) [12].

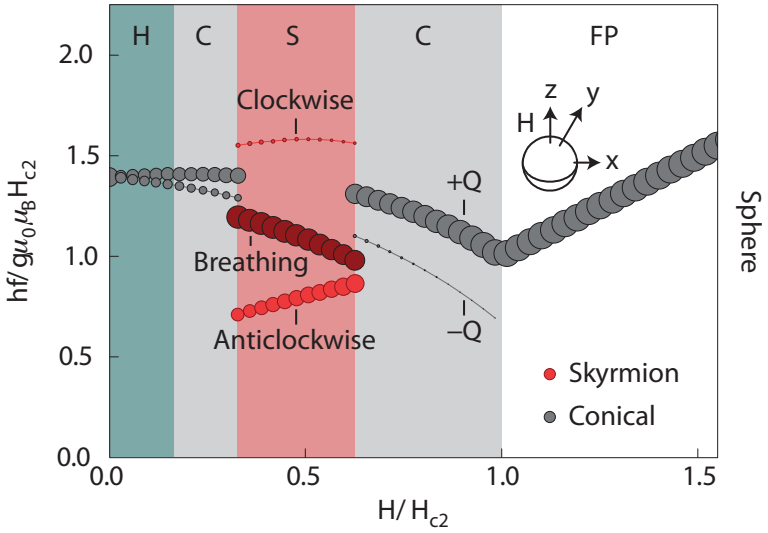

Figure 4: Excitation spectrum for a spherical sample [12].

1.2. Signature of the magnetic structure in neutron scattering experiments

When doing neutron scattering experiments to investigate the magnetic structure, one performs measurements in the momentum space.

In the conical phase one can observe two Bragg peaks, one at the north and one at the south pole of a sphere with radius Q. Q is determined by the constants of the theory (see section 2). Otherwise, when there is no magnetic field switched on, there is no preferred direction and the helices are pinned by anisotropies in the helical phase. Figure 5b shows the measured Bragg peaks in the conical phase. We notice that a helix in the conical phase is represented by two Bragg peaks in momentum space [13]. Figure 5a shows the FD regime at zero field where there is no preferred direction and hence the fluctuations are soft on the whole sphere [1].

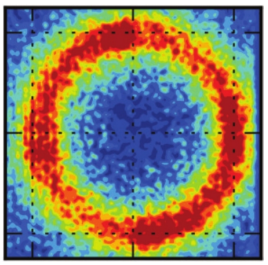

(a) FD regime at $B = 0$ [1]

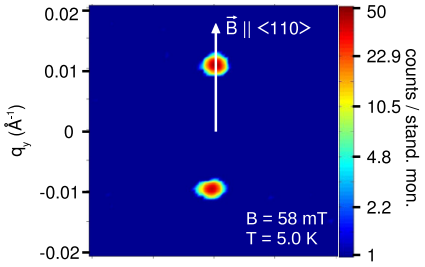

(b) Conical phase [13]

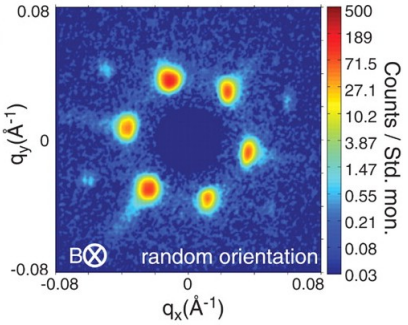

(c) Skyrmion phase [5]

Figure 5: Neutron scattering results in the different phases. In the FD regime at zero field (a) the fluctuations are soft on the whole sphere, in the conical phase (b) two Bragg peaks are located at the poles and in the skyrmionic phase (c) six Bragg peaks are lying in the plane perpendicular to the magnetic field.

When doing neutron scattering experiments in the skyrmion phase, one observes six main Bragg peaks lying in the equatorial plane (in contrast to the conical case where the peaks are located at the poles) as shown in figure 5c. They build a regular hexagon. Since we learned that a helix is represented by two Bragg peaks, one can identify the skyrmions with three helices. They lie in the equatorial plane and build an equilateral triangle with their pitch vectors as mentioned above [1, 5].

2. Ginzburg-Landau theory for chiral paramagnets

To describe chiral paragmagnets, one uses a Ginzburg-Landau theory, i. e. a ϕ^4-theory where ϕ is the order parameter of the system. The crystalline structures we consider here, for example of manganese silicide, are special since they do not obey inversion symmetry. MnSi builds a B20 structure, which is not inversion invariant. It occurs in two versions, a left-handed and a right-handed one, which is shown in figure 6 ([14]).

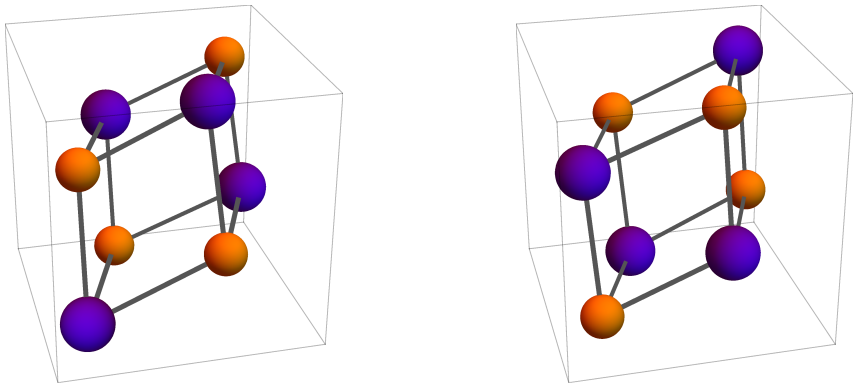

Figure 6: The lattice structure of MnSi exists in a left-handed and a right-handed version. Mn is represented by the violet spheres, Si by orange ones. [14]

Because of the lack of inversion symmetry, there is a further term allowed in the theory for chiral magnets, namely the Dzyaloshinskii-Moriya interaction [6, 7], which is of the form

$$D\vec{\phi}\cdot(\nabla\times\vec{\phi})\,. \tag{2.1}$$

The hole free energy density reads

$$\mathcal{F}=\frac{1}{2}\vec{\phi}\cdot(r-J\nabla^2)\vec{\phi}+D\vec{\phi}\cdot(\nabla\times\vec{\phi})+\frac{u}{4!}(\vec{\phi}^2)^2-\mu_0\mu\vec{\phi}\cdot\vec{H}\,. \tag{2.2}$$

The last term describes the coupling to an external magnetic field $\vec{H}$. The order parameter $\vec{\phi}$ is related to the magnetisation by the factor $\mu=\mu_B/\text{f.u.}$ with the formula unit f.u. $= 24.018\,\text{Å}^3$ for MnSi.

This whole section 2 follows the lines of [1].

2.1. Mean-field theory

One can now use mean-field theory to investigate the free energy density (2.2). In the simplest case one makes the ansatz $\vec{\phi}(\vec{x})=\phi_0\hat{H}$ and minimises the action with respect to ϕ_0 since in mean-field approximation the mean magnetisation points in the same direction as the magnetic field does. This ansatz is sufficient to describe the paramagnetic phase and the field polarised regime and leads to the mean-field

equation

$$r\phi_0 + \frac{u}{3!}\phi_0^3 = \mu_0\mu H\,. \tag{2.3}$$

For small fields, i. e. small ϕ_0, and $r > 0$ the first term of the left hand side is dominant. For ϕ_0 then

$$\phi_0 = \frac{\mu_0\mu H}{r} \tag{2.4}$$

holds. This is the case in the paramagnetic regime. For larger ϕ_0, the second term becomes the leading one. ϕ_0 is determined by

$$\phi_0 = \left(\frac{3!\,\mu_0\mu H}{u}\right)^{1/3}. \tag{2.5}$$

This is characteristic for the field polarised regime. The crossover between these two regimes is defined by the field where the two expressions for ϕ_0 are equal, namely

$$\mu_0\mu H = \sqrt{\frac{3!\,r^3}{u}}\,. \tag{2.6}$$

One can also introduce a helical element such that one can describe the conical phase with the following ansatz:

$$\vec{\phi}_{\mathrm{hel}}(\vec{x}) = \phi_0\hat{\phi}_0 + \psi_{\mathrm{hel}}\hat{e}^- e^{i\vec{Q}\cdot\vec{x}} + \psi^*_{\mathrm{hel}}\hat{e}^+ e^{-i\vec{Q}\cdot\vec{x}}\,. \tag{2.7}$$

Here $\hat{e}^\pm = (\hat{e}_1 \pm i\,\hat{e}_2)/\sqrt{2}$, where the pitch vector $\vec{Q}$ and $\hat{e}_1$ and $\hat{e}_2$ build a dreibein, i. e. $\hat{e}_1 \times \hat{e}_2 = \hat{Q}$. ψ_{hel} is the complex amplitude of the helical order. By plugging the ansatz (2.7) into the free energy (2.2), one arrives at the mean-field potential

$$\mathcal{V}_0 = \frac{r}{2}\,\phi_0^2 + \left(r + JQ^2 - 2DQ\right)|\psi_{\mathrm{hel}}|^2 + \frac{u}{4!}\left(\phi_0^2 + 2|\psi_{\mathrm{hel}}|^2\right)^2 - \mu_0\mu\,\phi_0\,H\,. \tag{2.8}$$

Minimising the potential with respect to the pitch length leads to the relation $D = JQ$.

One can now derive the susceptibility, whose inverse is defined by the second functional derivative of the action $S = \int d^3x\mathcal{F}/(k_BT)$ with respect to the magnetisation:

$$\chi^{-1}_{0,ij} = \frac{\delta^2 S}{\delta\vec{\phi}_i\delta\vec{\phi}_j}\,. \tag{2.9}$$

The index 0 is a reminder that one still remains in the mean-field approximation. In real space the inverse susceptibility reads

$$\begin{aligned}\chi^{-1}_{0,ij}(\vec{x},\vec{x}') =& \frac{1}{k_BT}\Bigg[\Big(r - J\nabla^2\Big)\delta_{ij} - 2D\epsilon_{ijn}\nabla_n \\ &+ \frac{u}{3!}\left(\vec{\phi}(\vec{x})^2\delta_{ij} + 2\vec{\phi}_i(\vec{x})\vec{\phi}_j(\vec{x})\right)\Bigg]\delta\big(\vec{x} - \vec{x}'\big)\,.\end{aligned} \tag{2.10}$$

Performing a Fourier transformation and considering only the part diagonal in

momenta leads to

$$\chi^{-1}_{0,ij}(\vec{k}) = \frac{1}{k_B T}\Bigg[\Big(r + J\vec{k^2}\Big)\delta_{ij} - i\,2D\,\epsilon_{ijn}\vec{k}_n + \frac{u}{3!}\,\phi_0^2\Big(\delta_{ij} + 2\hat{\phi}_{0,i}\hat{\phi}_{0,j}\Big) + \frac{u}{3}\,|\psi_{\mathrm{hel}}|^2\Big(2\delta_{ij} - \hat{Q}_i\hat{Q}_j\Big)\Bigg]. \tag{2.11}$$

Going back to the free energy density, one can see that, when coupling one of the ϕ in the ϕ^4-term of the free energy (2.2) to the mean field ϕ_0, the system can gain energy when the momentum vectors of the remaining $\phi(\vec{q})$ build a triangle. This term is of the form

$$\sum_{\vec{q}_1,\vec{q}_2,\vec{q}_3} \Big(\vec{\phi}_0 \cdot \vec{\phi}(\vec{q}_1)\Big)\,\Big(\vec{\phi}(\vec{q}_2) \cdot \vec{\phi}(\vec{q}_3)\Big)\;\delta\big(\vec{q}_1 + \vec{q}_2 + \vec{q}_3\big)\,. \tag{2.12}$$

As described in [5], for the skyrmion phase it is appropriate to make the ansatz

$$\vec{\phi}(\vec{x}) = \vec{\phi}_0 + \sum_{i=1}^{3} \vec{\phi}^{\,i}_{\mathrm{hel}}\big(\vec{x} + \Delta\vec{x}_i\big)\,. \tag{2.13}$$

$\vec{\phi}_{\mathrm{hel}}$ corresponds to the helical ansatz (2.7) without the constant term $\phi_0\hat{\phi}_0$ and with the pitch vectors $\vec{Q}_i$:

$$\vec{\phi}^{\,i}_{\mathrm{hel}}(\vec{x}) = A\Big[\hat{n}^i_1 \cos\Big(\vec{Q}_i \cdot \vec{x}\Big) + \hat{n}^i_2 \sin\Big(\vec{Q}_i \cdot \vec{x}\Big)\Big]\,. \tag{2.14}$$

A is the amplitude. $\hat{n}^i_1$, $\hat{n}^i_2$ and $\vec{Q}_i$ build a dreibein with the same orientation for all i. This ansatz corresponds to three superposing helices. The relative shifts of the helices $\Delta\vec{x}_i$ determine the magnetic structure, i. e. whether there is a skyrmion lattice or something else. For a skyrmion lattice the three pitch vectors build an equilateral triangle in a plane perpendicular to the external magnetic field, i. e. the direction of $\vec{\phi}_0$.

2.2. Brazovskii theory

Mean-field theory predicts a second order phase transition between the paramagnetic phase and the magnetically ordered phases. One has to include fluctuations to understand the first order transition which is observed experimentally. Fluctuations are included by doing perturbation theory.

In the 80s Brazovskii, Dzyaloshinskii and Muratov investigated phase transitions and crystallisation. In [15] they describe the formation of different dimensional crystalline structures. In the case of chiral magnets, one has periodic magnetic structures in one and two dimensions. The skyrmion lattice is two dimensional because of the triangular lattice in 2d. In the third direction there is no periodic structure but translational invariance. In contrast, the helical phase is only periodic

in one direction, so it forms a 1d structure. Therefore, we can use Brazovskii's theory to describe chiral paramagnets [15, 16].

Brazovskii found that triangular configurations of the momentum vectors played an important role in the investigated crystallisation processes (cf. figure 1 in [15]).

In [1] the authors choose a parametrisation such that the propagator looks like

$$\chi_{ij}^{-1}(\vec{k}) = \frac{1}{k_B T}\left[\left(JQ^2 + J\vec{k}^2\right)\delta_{ij} - i2D\epsilon_{ijn}\vec{k}_n + \Delta_\perp\left(\delta_{ij} - \hat{n}_i\hat{n}_j\right) + \Delta_\parallel \hat{n}_i\hat{n}_j\right] . \quad (2.15)$$

$\Delta_\perp$ and $\Delta_\parallel$ are variational parameters for which they derive self-consistent equations. This derivation will be sketched in the following. In the paramagnetic phase $\hat{n}$ denotes the direction of the magnetic field. For a finite magnetic field it holds $\Delta_\parallel > \Delta_\perp$. We will show in subsection 4.2 that the Δ_i, with $i \in \{\perp, \parallel\}$, are related to the energy gaps in the different directions in momentum space.

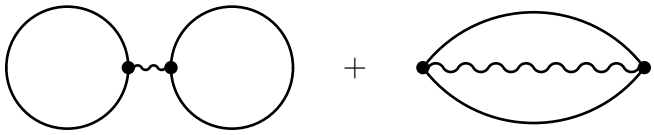

Figure 7: Hartree-Fock diagrams

To include fluctuations, one derives self-consistency equations for the energy gaps by including the Hartree-Fock terms. The diagrammatic approach is shown in figure 7. This leads to an additional term in the action of the form

$$\Gamma_2 = \frac{u}{4! k_B T}\int d\vec{x}\left[\left(\operatorname{Tr}\chi(\vec{x},\vec{x})\right)^2 + 2\operatorname{Tr}\chi^2(\vec{x},\vec{x})\right] . \quad (2.16)$$

The whole effective two-particle irreducible action is derived by Cornwall, Jackiw and Tomboulis in [17]:

$$S_{\text{eff}}[\vec{\phi},\chi] = S[\vec{\phi}] + \frac{1}{2}\operatorname{Tr}\log\chi^{-1} + \frac{1}{2}\operatorname{Tr}\left(\chi_0^{-1} - \chi^{-1}\right)\chi + \Gamma_2[\vec{\phi},\chi] . \quad (2.17)$$

$S[\vec{\phi}]$ is the original action with the free energy density (2.2). χ_0 is the mean-field susceptibility. $\vec{\phi}$ and χ are defined by minimising the effective action with respect to each of them.

Plugging the mean-field ansatz in the conical phase (2.7) for $\vec{\phi}$ and the ansatz for the susceptibility (2.15) into (2.17) allows to write down the effective potential,

which is related to the effective action by $S_{\text{eff}} = V\mathcal{V}_{\text{eff}}/(k_B T)$:

$$\begin{aligned}\mathcal{V}_{\text{eff}} =& \left[\frac{r}{2}\,\phi_0^2 + \left(r + JQ^2 - 2DQ\right)|\psi_{\text{hel}}|^2 + \frac{u}{4!}\left(\phi_0^2 + 2|\psi_{\text{hel}}|^2\right)^2 - \mu_0\mu\,\phi_0\,H\right] \\ &+ \frac{1}{2}\,D(\Delta_\perp, \Delta_\parallel) + \frac{1}{2}\left[\left(r - JQ^2\right) + \frac{u}{3!}\left(\phi_0^2 + 4|\psi_{\text{hel}}|^2\right) - \Delta_\perp\right] D_\perp \\ &+ \frac{1}{2}\left[\left(r - JQ^2\right) + \frac{u}{3!}\left(3\phi_0^2 + 2|\psi_{\text{hel}}|^2\right) - \Delta_\parallel\right] D_\parallel \\ &+ \frac{u}{4!}\left[(D_\perp + D_\parallel)^2 + 2\left(\frac{1}{2}D_\perp^2 + D_\parallel^2\right)\right], \end{aligned} \tag{2.18}$$

with the function

$$D(\Delta_\perp, \Delta_\parallel) = k_B T \int \frac{d\vec{k}}{(2\pi)^3} \log\det \chi^{-1}(\vec{k})\,. \tag{2.19}$$

$D_\perp$ ($D_\parallel$) denotes the derivative of D with respect to $\Delta_\perp$ ($\Delta_\parallel$).

Varying the effective potential with respect to the energy gaps Δ_i leads to self-consistency equations for them, the generalised Brazovskii equations:

$$\Delta_\perp = \left(r - JQ^2\right) + \frac{u}{3!}\left(\phi_0^2 + 4|\psi_{\text{hel}}|^2\right) + \frac{u}{3!}\left(2D_\perp + D_\parallel\right), \tag{2.20}$$

$$\Delta_\parallel = \left(r - JQ^2\right) + \frac{u}{3!}\left(3\phi_0^2 + 2|\psi_{\text{hel}}|^2\right) + \frac{u}{3!}\left(D_\perp + 3D_\parallel\right). \tag{2.21}$$

In subsection 4.2 we will take a closer look at the physical meaning of the energy gaps and compare the results of these equations with some experimental data.

Part III.
Susceptibility in the fluctuation disordered regime

In this part we will present the calculation of the susceptibility in a perturbative approach. For this, we will calculate the self-energy up to the second order diagram and determine the imaginary part of the susceptibility within this approximation.

There is some experimental motivation to do this calculation. In the group of Prof. Dirk Grundler and Prof. Christian Pfleiderer at the Technische Universität München resonance experiments were performed by Ioannis Stasinopoulos. He observes deviations from the ferromagnetic resonance frequency $\omega_{\text{ferro}} = g\mu_B B/\hbar$ in the fluctuation-disordered regime [4].

This is shown in figure 8. The left plot shows the path through the phase diagram, which was used, and the red dots on the right hand side show the peak positions. The green triangles are the widths of the peaks. They are nearly of the same order as the peaks. Thus, the observed peaks are not sharp resonances. The gray line in the field polarised (FP) region denotes ω_{ferro}. When entering the fluctuation disordered regime, the gray line now denotes the positions of excitations, which one would expect in the conical phase. The red lines show where the skyrmionic gyration modes would be located in the skyrmion phase (cf. figure 4). The breathing mode is only excited by a varying magnetic field parallel to the static magnetic field and can, therefore, not be observed here [12].

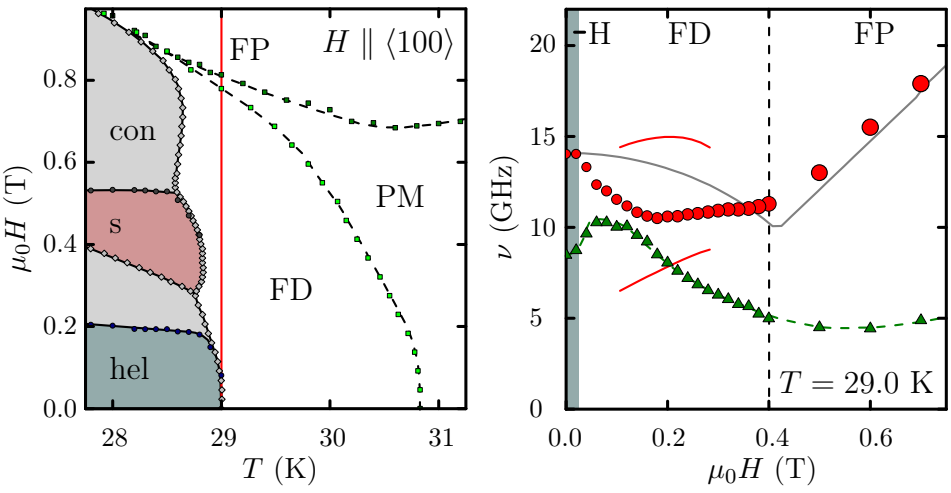

Figure 8: Experimental data (I. Stasinopoulos) [4]. The red line in the left picture shows a path through the phase diagram for a fixed temperature. This path is taken in the right plot, which shows the measured resonance frequencies (red dots) as a function of magnetic field and the corresponding FWHM (green triangles) at 29 K.

The experiments show a deviation from ω_{ferro} to higher frequencies [4]. The question is if this can be explained by the calculation presented in the following chapters.

The weight of the ferromagnetic resonance goes down with decreasing magnetic field since it is proportional to the magnetic field strength B. The question is whether we can find processes which then can gain influence but are suppressed for higher magnetic fields. Since the skyrmion excitation frequencies, especially the anticlockwise gyration mode, lie above ω_{ferro}, skyrmion type fluctuations could be a candidate to explain the resonance shift.

The calculation presented in the rest of this thesis is only valid in a certain range of magnetic field and temperature, namely in the fluctuation-disordered regime where the Brazovskii theory can be used. Furthermore, the explicit form of the dynamical term is only valid for finite magnetic fields. For zero magnetic field it exhibits a divergence and therefore cannot be used in this form anymore.

3. Electron-spin resonance and precessional dynamics

To describe chiral paramagnets like MnSi, we use the Ginzburg-Landau theory for chiral magnets described in section 2. Since we are interested in resonances, we also have to include dynamics in the theory. We restrict ourselves to precessional dynamics and neglect any damping terms.

The equation of motion for the magnetisation is

$$\frac{d\vec{M}}{dt} = -\gamma \, \vec{M} \times \vec{B} \, . \tag{3.1}$$

γ is the positive gyromagnetic ratio. This leads to the resonance frequency

$$\omega_{\text{ferro}} = \frac{g\mu_B B}{\hbar} \, , \tag{3.2}$$

with the g-factor g and the Bohr magneton μ_B. This frequency is also a benchmark and should be recovered by the case $\vec{q} = 0$ in the dynamical Ginzburg-Landau theory. With this in mind, it is possible to derive the exact form of the precession term in the inverse Green's function, which we present in this chapter.

3.1. Electron-spin resonance frequency

In this section we will derive the electron-spin resonance at a finite magnetic field in the quantum field theory language which is used in this thesis. We set $\hbar = 1$. In the paramagnetic regime, where the electron-spin resonance occurs, the Dzyaloshinskii-Moriya interaction is negligible. Therefore, the Lagrange density for

fermions is

$$\mathcal{L}[\psi^\dagger,\psi] = \psi^\dagger\big(\partial_\tau+\epsilon\big)\psi + \tilde{J}\left(\psi^\dagger\frac{\vec{\sigma}}{2}\psi\right)^2 + g\mu_B\left(\psi^\dagger\frac{\vec{\sigma}}{2}\psi\right)\cdot\vec{B}\,. \tag{3.3}$$

To distinguish the parameter J from the one in the theory for chiral magnets, the former is marked by a tilde.

To get rid of the quartic term in the fermionic fields, i. e. the $\left(\psi^\dagger\frac{\vec{\sigma}}{2}\psi\right)^2$-term, we introduce a bosonic field $\vec{\varphi}$ by performing a Hubbard-Stratonovich transformation,

$$\mathcal{L}[\psi^\dagger,\psi,\vec{\varphi}] = \psi^\dagger\big(\partial_\tau+\epsilon\big)\psi + \left(\psi^\dagger\frac{\vec{\sigma}}{2}\psi\right)\cdot\vec{\varphi} - \frac{1}{4\tilde{J}}\vec{\varphi}^2 + g\mu_B\left(\psi^\dagger\frac{\vec{\sigma}}{2}\psi\right)\cdot\vec{B}\,. \tag{3.4}$$

The Hubbard-Stratonovich field corresponds, therefore, to

$$\vec{\varphi} = \tilde{J}\psi^\dagger\vec{\sigma}\psi\,. \tag{3.5}$$

We want to shift $\vec{\varphi}$ such that it couples to the magnetic field instead of $\psi^\dagger\frac{\vec{\sigma}}{2}\psi$, i. e. $\vec{\varphi}\to\vec{\varphi}-g\mu_B\vec{B}$. Then we obtain the Lagrange density

$$\mathcal{L}[\psi^\dagger,\psi,\vec{\varphi}] = \psi^\dagger\big(\partial_\tau+\epsilon\big)\psi + \left(\psi^\dagger\frac{\vec{\sigma}}{2}\psi\right)\cdot\vec{\varphi} - \frac{1}{4\tilde{J}}\vec{\varphi}^2 + \frac{g\mu_B}{2\tilde{J}}\vec{\varphi}\cdot\vec{B} - \frac{(g\mu_B)^2}{4\tilde{J}}\vec{B}^2. \tag{3.6}$$

Now, it is obvious that the order parameter $\vec{\varphi}$ corresponds to the magnetisation, which one can read off from the penultimate term since the magnetisation couples linearly to the magentic field and without any factor by definition,

$$\vec{M} = -\frac{g\mu_B}{2\tilde{J}}\vec{\varphi}\,. \tag{3.7}$$

One can thus rewrite the Lagrange density using the magnetisation instead of $\vec{\varphi}$,

$$\mathcal{L}[\psi^\dagger,\psi,\vec{M}] = \psi^\dagger\big(\partial_\tau+\epsilon\big)\psi - \frac{2\tilde{J}}{g\mu_B}\left(\psi^\dagger\frac{\vec{\sigma}}{2}\psi\right)\cdot\vec{M} - \frac{\tilde{J}}{(g\mu_B)^2}\vec{M}^2 - \vec{M}\cdot\vec{B} - \frac{(g\mu_B)^2}{4\tilde{J}}\vec{B}^2. \tag{3.8}$$

Integrating out the fermionic fields and switching to momentum and frequency space leads to the effective Lagrange density

$$\mathcal{L}[\vec{\varphi}] = \frac{1}{2}\,\vec{\varphi}^T(G^{-1})\vec{\varphi} + \frac{g\mu_B}{2\tilde{J}}\,\vec{\varphi}\cdot\vec{B} - \frac{(g\mu_B)^2}{4\tilde{J}}\,\vec{B}^2. \tag{3.9}$$

The inverse Green's function at finite momentum $\vec{q}$ is defined as

$$G^{-1}(\vec{q},\Omega) = -\frac{1}{2\tilde{J}}+\Pi = \left(-\frac{1}{2\tilde{J}}-\frac{\nu}{2}\right)\mathbb{1}+\frac{\nu\pi}{4}\frac{|\Omega|}{|\vec{q}|}\begin{pmatrix}0&0&0\\0&0&0\\0&0&1\end{pmatrix}+i\nu\frac{i\Omega}{2\varphi_0}\begin{pmatrix}0&-1&0\\1&0&0\\0&0&0\end{pmatrix} \tag{3.10}$$

with Π being the self-energy and ν the density of states. $\vec{\varphi}$ is, therefore, the field

which describes the fluctuations. It has a finite frequency Ω. This expression is only valid for $\Omega < |\vec{q}|$. φ_0, on the other hand, which occurs in the Green's function, corresponds to the homogeneous component of the magnetisation, i. e. the mean magnetisation at a finite magnetic field. It is given by $\vec{M}_0 = \chi(\Omega = 0)\vec{B}$. This explicit form can only be used for a finite mean magnetisation, which corresponds to a finite magnetic field. Otherwise, there will occur a divergence in the Green's function. For the case of zero magnetic field, the derivation of the Green's function cannot be done this way. The explicit form of the self-energy is derived in [18]. The derivation is sketched in Appendix A.

For the stationary case, i. e. $\Omega = 0$, it is possible to calculate the susceptibility simply by integrating out the Hubbard-Stratonovich field. The Lagrangian for $\Omega = 0$ reads

$$\mathcal{L}[\vec{\varphi}] = -\frac{1+\tilde{J}\nu}{4\tilde{J}}\,\vec{\varphi}^2 + \frac{g\mu_B}{2\tilde{J}}\,\vec{\varphi}\cdot\vec{B} - \frac{(g\mu_B)^2}{4\tilde{J}}\,\vec{B}^2\,. \tag{3.11}$$

By shifting the field $\vec{\varphi} \to \vec{\varphi} + \frac{g\mu_B}{1+\tilde{J}\nu}\vec{B}$, we can directly integrate out $\vec{\varphi}$ and get

$$\mathcal{L}_{\text{eff}}[\vec{B}] = \frac{(g\mu_B)^2}{4\tilde{J}}\left(\frac{1}{1+\tilde{J}\nu} - 1\right)\vec{B}^2 \equiv -\frac{1}{2}\,\vec{B}^T\chi(\Omega = 0)\vec{B}\,. \tag{3.12}$$

It follows that the susceptibility for the stationary case reads

$$\chi(\Omega = 0) = \frac{(g\mu_B)^2}{2}\,\frac{\nu}{1+\tilde{J}\nu}\,. \tag{3.13}$$

Now, let us switch on dynamics. For that we go back to the Lagrange density

$$\mathcal{L}[\vec{\varphi}] = \frac{1}{2}\vec{\varphi}^T(G^{-1})\vec{\varphi} + \frac{g\mu_B}{2\tilde{J}}\,\vec{\varphi}\cdot\vec{B} - \frac{(g\mu_B)^2}{4\tilde{J}}\,\vec{B}^2\,. \tag{3.14}$$

By shifting the field $\vec{\varphi} \to \vec{\varphi} + \frac{g\mu_B}{2\tilde{J}}G$, the bosonic fields $\vec{\varphi}$ can be integrated out like before, except for the zero mode since it is also present in the Green's function. The effective Lagrangian for the magnetic field reads

$$\mathcal{L}_{\text{eff}}[\vec{B}] = -\frac{1}{2}\left[\left(\frac{g\mu_B}{2\tilde{J}}\right)^2\vec{B}^T G\vec{B} + \frac{(g\mu_B)^2}{4\tilde{J}}\vec{B}^2\right]. \tag{3.15}$$

Inverting the inverse Green's function leads to the propagator

$$G = \frac{1}{\left(\frac{1+\tilde{J}\nu}{2\tilde{J}}\right)^2 - \left(\nu\frac{i\Omega}{2\varphi_0}\right)^2}\begin{pmatrix} -\frac{1+\tilde{J}\nu}{2\tilde{J}} & i\nu\frac{i\Omega}{2\varphi_0} & 0 \\ -i\nu\frac{i\Omega}{2\varphi_0} & -\frac{1+\tilde{J}\nu}{2\tilde{J}} & 0 \\ 0 & 0 & 0 \end{pmatrix} + \frac{1}{-\frac{1}{2\tilde{J}} - \frac{\nu}{2} + \frac{\nu\pi|\Omega|}{4|\vec{q}|}}\begin{pmatrix} 0 & 0 & 0 \\ 0 & 0 & 0 \\ 0 & 0 & 1 \end{pmatrix}. \tag{3.16}$$

The susceptibility can be read off when remembering that $\mathcal{L} = \frac{1}{2}\vec{B}^T\chi\vec{B}$ holds for

the Lagrangian.

$$\chi = \left(\frac{g\mu_B}{2\tilde{J}}\right)^2 \left[\frac{1}{\left(\frac{1+\tilde{J}\nu}{2\tilde{J}}\right)^2 - \left(\nu\frac{i\Omega}{2\varphi_0}\right)^2} \begin{pmatrix} -\frac{1+\tilde{J}\nu}{2J} & i\nu\frac{i\Omega}{2\varphi_0} & 0 \\ -i\nu\frac{i\Omega}{2\varphi_0} & -\frac{1+\tilde{J}\nu}{2\tilde{J}} & 0 \\ 0 & 0 & 0 \end{pmatrix} \right.$$
$$\left. + \frac{1}{-\frac{1}{2\tilde{J}} - \frac{\nu}{2} + \frac{\nu\pi|\Omega|}{4|\vec{q}|}} \begin{pmatrix} 0 & 0 & 0 \\ 0 & 0 & 0 \\ 0 & 0 & 1 \end{pmatrix} + 2\tilde{J}\mathbb{1} \right] . \tag{3.17}$$

Where does the susceptibility exhibit divergences? With analytic continuation $i\Omega \to \omega + i0^+$ we obtain the resonance frequency

$$\omega_{\text{ferro}} = \pm\frac{1+\tilde{J}\nu}{\tilde{J}\nu}\,\varphi_0\,, \tag{3.18}$$

where φ_0 is the magnetisation at zero frequency. One cannot put in the mean-field defined expression which is obtained by varying the action with respect to φ_0. Instead, we have to use the full one given by the susceptibility. Using $\vec{M}_0 = \chi(\Omega = 0)\vec{B}$ and what we calculated above for the susceptibility $\chi(0)$, we can replace φ_0 by $\varphi_0 = -2\tilde{J}/(g\mu_B)\chi(0)\cdot B$ and finally obtain the expected resonance frequency for electron-spin resonance (Lamor frequency):

$$\omega_{\text{ferro}} = g\mu_B B\,. \tag{3.19}$$

3.2. Green's function with precessional dynamics

We want to derive the pre-factor of the precession term in the Green's function of the Ginzburg-Landau theory for chiral paramagnets. From the calculation of the electron-spin resonance (cf. subsection 3.1) we know that it should have a form similar to $i\,\nu/(2\phi_0)$. However, this cannot be adopted directly since the susceptibility is defined by other constants. Even the field ϕ is not the same as φ in the electron-spin calculation. Also note that the $\tilde{J}$ from the electron-spin resonance calculation does not correspond to the one in the Ginzburg-Landau theory for chiral magnets.

Furthermore, we will neglect the damping term proportional to $|\Omega|/|\vec{q}|$ in the inverse Green's function in the following.

The correlation between the magnetisation $\vec{M}$ and the field $\vec{\varphi}$ was already derived in subsection 3.1 and reads

$$\vec{M} = -\frac{g\,\mu_B}{2\tilde{J}}\vec{\varphi}\,. \tag{3.20}$$

We also know the correlation between the magnetisation and $\vec{\phi}$, which we can read off from the term that couples $\vec{\phi}$ to the external magnetic field in the free energy

density (2.2). This is given explicitly in [1]:

$$\vec{M} = \frac{\mu_B}{\text{f.u.}} \vec{\phi} \,. \tag{3.21}$$

The formula unit is f.u. = 24.018 Å^3 for MnSi. Therefore, we arrive at

$$\vec{\varphi} = -\frac{2\tilde{J}}{g\,\text{f.u.}} \vec{\phi} \,. \tag{3.22}$$

In the case of chiral magnets the precession term has a pre-factor of the form

$$\left(\frac{2\tilde{J}}{g\,\text{f.u.}} \right)^2 \frac{i\nu}{2\varphi_0} =: i\,n \,. \tag{3.23}$$

With the expression (3.20) above, we can substitute φ_0 with the mean magnetisation, for which holds $M_0 = \chi_0 B$. Furthermore, we introduce the conical susceptibility χ_{con} in mean-field approximation:

$$\chi_{\text{con}} = \frac{\mu_0\,\mu_B^2}{JQ^2\,(\text{f.u.})^2} \tilde{J}\nu \,. \tag{3.24}$$

Note that it is a constant in the conical phase [19]. This allows us to write

$$i\,n = i\,\frac{\chi_{\text{con}}}{\chi_0} \frac{1}{\omega_{\text{ferro}}} \tag{3.25}$$

where

$$\omega_{\text{ferro}} = g\mu_B B \tag{3.26}$$

as shown before (with $\hbar = 1$).

For $\vec{q} = 0$ we should recover the electron-spin resonance frequency ω_{ferro} from the inverse Green's function. The latter is given by equation (2.15). Here, all momenta are measured in units of Q and the factor JQ^2 was factored out and dropped. In the following we will calculate everything with dimensionless quantities. The units will be recovered at the very end. The parameters $\Delta_\perp$ and $\Delta_\parallel$ are replaced by the parameters $\kappa_\perp$ and $\kappa_\parallel$, which have the dimension of a momentum and are thus measured in units of Q, too. The relation between the Δ_i and the κ_i is given by $\Delta_i = JQ^2\kappa_i^2$.

We consider the inverse Green's function in the limit $\vec{q} = 0$:

$$G^{-1}(0,\omega) = \begin{pmatrix} 1+\kappa_\perp^2 & -i\frac{\chi_{\text{con}}}{\chi_0}\frac{i\omega}{\omega_{\text{ferro}}} & 0 \\ i\frac{\chi_{\text{con}}}{\chi_0}\frac{i\omega}{\omega_{\text{ferro}}} & 1+\kappa_\perp^2 & 0 \\ 0 & 0 & 1+\kappa_\parallel^2 \end{pmatrix} \,. \tag{3.27}$$

From $\det G^{-1} = 0$ follows

$$\omega_{\text{res}} = \frac{\chi_0}{\chi_{\text{con}}} \left(1 + \kappa_\perp^2\right) \omega_{\text{ferro}} \stackrel{!}{=} \omega_{\text{ferro}} \; . \tag{3.28}$$

We can conclude that $\frac{\chi_0}{\chi_{\text{con}}} = \frac{1}{1+\kappa_\perp^2}$. We arrive at the dimensionless inverse Green's function

$$G^{-1}(\vec{q}, \Omega) = \begin{pmatrix} 1 + q^2 + \kappa_\perp^2 & -i\left(1 + \kappa_\perp^2\right)(i\Omega) - 2iq_3 & 2iq_2 \\ i\left(1 + \kappa_\perp^2\right)(i\Omega) + 2iq_3 & 1 + q^2 + \kappa_\perp^2 & -2iq_1 \\ -2iq_2 & 2iq_1 & 1 + q^2 + \kappa_\parallel^2 \end{pmatrix} , \tag{3.29}$$

where the frequencies are measured in units of ω_{ferro}, i. e. $\Omega = \omega/\omega_{\text{ferro}}$, and all momenta are in units of Q.

When performing the calculation in the limit of $\vec{q} = 0$ to extract the ferromagnetic resonance frequency, we can also calculate the weight of this resonance. It corresponds to the pre-factor of the delta function $\delta(\omega - \omega_{\text{ferro}})$. It reads

$$\text{Weight}_{\text{ESR}} = \frac{\pi}{2} \frac{1}{JQ^2} \frac{\omega_{\text{ferro}}}{1 + \kappa_\perp^2} \; . \tag{3.30}$$

Since ω_{ferro} is proportional to B, the ESR weight is propotional to B, and therefore vanishes for $B \to 0$. Scattering processes including multiple magnons could gain importance in the limit of small magnetic fields.

4. Spectrum of the non-interacting system

As we have seen in the previous sections, the propagator has the following form:

$$G^{-1}(\vec{q},\Omega) = \begin{pmatrix} 1+q^2+\kappa_\perp^2 & -i\,(1+\kappa_\perp^2)\,(i\Omega) - 2iq_3 & 2iq_2 \\ i\,(1+\kappa_\perp^2)\,(i\Omega) + 2iq_3 & 1+q^2+\kappa_\perp^2 & -2iq_1 \\ -2iq_2 & 2iq_1 & 1+q^2+\kappa_\parallel^2 \end{pmatrix} . \tag{4.1}$$

The aim of this chapter is to understand this Green's function better and get a feeling for the physical meaning of $\kappa_\perp$ and $\kappa_\parallel$.

4.1. Static case without magnetic field

First, we consider the static case, i. e. $\Omega = 0$. When there is no external magnetic field, there is no preferred direction in the system, which means that $\kappa_\perp = \kappa_\parallel \equiv \kappa$. The inverse Green's function for this case reads

$$G^{-1}(\vec{q},0) = \begin{pmatrix} 1+q^2+\kappa^2 & -2iq_3 & 2iq_2 \\ 2iq_3 & 1+q^2+\kappa^2 & -2iq_1 \\ -2iq_2 & 2iq_1 & 1+q^2+\kappa^2 \end{pmatrix} . \tag{4.2}$$

The spectrum consists of three modes, namely

$$\lambda_1 = \kappa^2 + \big(|\vec{q}| - 1\big)^2, \tag{4.3}$$

$$\lambda_2 = \kappa^2 + \big(|\vec{q}| + 1\big)^2, \tag{4.4}$$

$$\lambda_3 = \kappa^2 + \vec{q}^{\,2} + 1 \; . \tag{4.5}$$

Figure 9 shows the spectrum as a function of $q = |\vec{q}|$. We observe that the energy gap of the spectrum is determined by κ^2. Remember that the momenta are measured in units of $Q = D/J$. The minimum of λ_1 is on a sphere in momentum space with radius $|\vec{q}| = 1$, which thus corresponds to Q.

When calculating the Hartree-Fock term to investigate the fluctuation-disordered regime (cf. subsection 2.2), as it is done in [1], one has to integrate over the Green's function. This corresponds to an integration over the inverse of the eigenvalues $1/\lambda_i$. For $\kappa \to 0$, the first eigenvalue is of special interest since it vanishes for $|\vec{q}| \to 1$. This results in a $1/\kappa$-divergence since

$$\int d\vec{q}\, \frac{1}{\kappa^2 + (|\vec{q}| - 1)^2} \sim \alpha + \frac{\beta}{\kappa} \tag{4.6}$$

in leading order for small $\kappa \ll 1$. α and β are real and finite constants. This leads to the Brazovskii equation, the self-consistency equation for the momentum

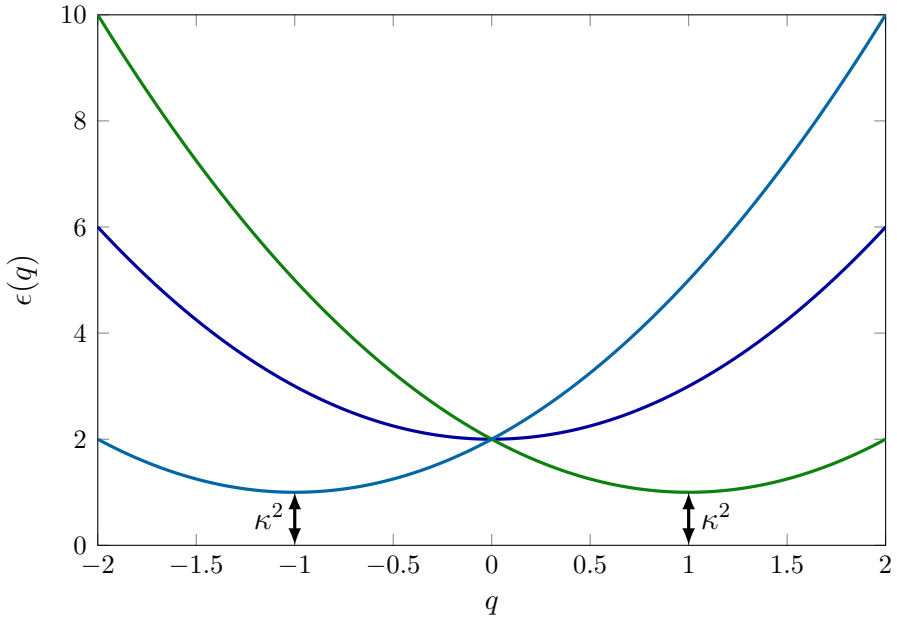

Figure 9: Spectrum for $\Omega = 0$ and $\vec{B} = 0$

κ corresponding to the energy gap:

$$\kappa^2 = \kappa_{\mathrm{MF}}^2 + \frac{\kappa_{\mathrm{Gi}}^3}{\kappa} \,, \tag{4.7}$$

where κ_{Gi} is constant and $\kappa_{\mathrm{MF}} \propto (T - T_{\mathrm{MF}})$. For vanishing magnetic field the generalised Brazovskii equations (2.21) and (2.20) simplify to the Brazovskii equation (4.7) [1].

That means that for $\kappa \to 0$ the fluctuations become soft on a sphere in momentum space with radius Q. Figure 10a shows exactly this sphere. The colour is related to the value of $\mathrm{Tr}\, G$. Red corresponds to a high value and blue to a low one. We observe that the whole sphere is red, i. e. $\mathrm{Tr}\, G$ is divergent on the whole sphere. This is also observed in neutron scattering experiments shown in figure 10b [1].

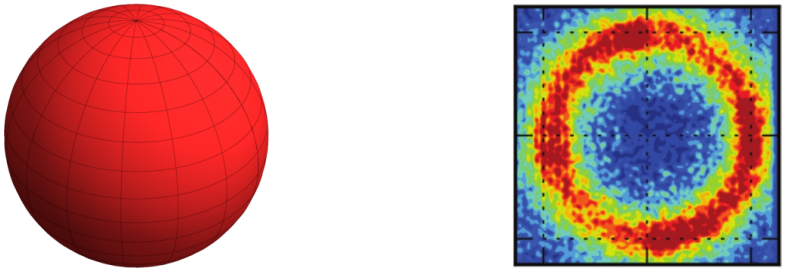

(a) (b)

Figure 10: (a) $\mathrm{Tr}\, G(\vec{q}, 0)$ at $\vec{B} = 0$ plotted on a sphere in momentum space with radius Q. (b) shows experimental data where one can observe the fluctuations becoming soft on the sphere [1, 3].

4.2. Static case with magnetic field

Now we switch on the external magnetic field but still remain in the static limit, i. e. $\Omega = 0$. We choose the magnetic field to point in z-direction. The inverse Green's function reads

$$G^{-1}(\vec{q}, 0) = \begin{pmatrix} 1 + q^2 + \kappa_\perp^2 & -2iq_3 & 2iq_2 \\ 2iq_3 & 1 + q^2 + \kappa_\perp^2 & -2iq_1 \\ -2iq_2 & 2iq_1 & 1 + q^2 + \kappa_\parallel^2 \end{pmatrix} . \tag{4.8}$$

The self-consistency equations for the energy gaps $\Delta_{\perp/\parallel}$ are derived in [1] which is described in subsection 2.2. The relation between the parameters $\Delta_{\perp/\parallel}$ and $\kappa_{\perp/\parallel}$ is $\Delta_{\perp/\parallel} = JQ^2\kappa_{\perp/\parallel}^2$. Again, we examine the spectrum presented in figure 11. There are two different cases. If the momentum vector $\vec{q}$ is parallel to the magnetic field, there is a small gap $\kappa_\perp^2$ (cf. figure 11a). The minimum is located at $|\vec{q}| = 1$. When $\vec{q}$ is perpendicular to $\vec{B}$, the gap Δ is bigger (cf. figure 11b). It is not simply $\kappa_\parallel^2$ but has a more complex form, namely

$$\Delta = \frac{1}{16}\left(8\left(\kappa_\perp^2 + \kappa_\parallel^2\right) - \left(\kappa_\parallel^2 - \kappa_\perp^2\right)^2\right) . \tag{4.9}$$

The position of the minimum is also slightly shifted.

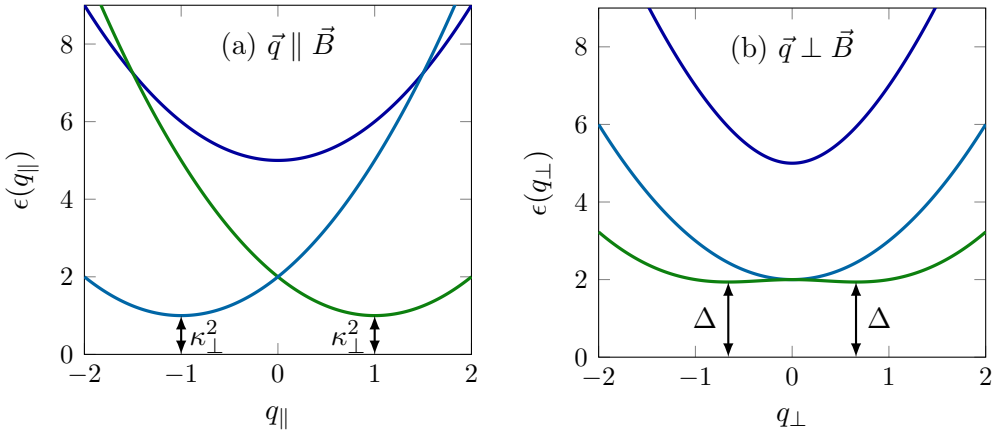

Figure 11: Spectrum for $\vec{q}$ pointing in different directions: (a) $\vec{q} \parallel \vec{B}$ and (b) $\vec{q} \perp \vec{B}$ for $(\kappa_\parallel, \kappa_\perp) = (2.0, 1.0)$.

When increasing the magnetic field, we observe that the weight of $\operatorname{Tr} G$ accumulates at the poles and finally ends up in the conical phase as shown in figure 5b for the experimental case. This process is illustrated in figure 12. The left sphere is plotted without magnetic field. Moving to the right, the magnetic field increases from sphere to sphere.

$\kappa_{\perp/\parallel}$ can be measured. The respective experiments were performed by Jonas Kindervater in the group of Prof. C. Pfleiderer at the Technische Universität in Munich. One can compare the generalised Brazovskii equations (2.21) and (2.20) to

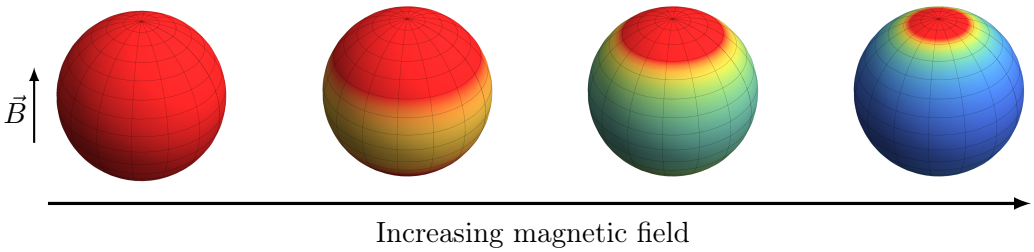

Figure 12: $\mathrm{Tr}\, G(\vec{q})$ with $|\vec{q}| = 1$ for an increasing magnetic field

the experimental data. This is done by using $J \approx 2.8\,\mathrm{meV/\AA}$ and $Q \approx 0.039\,\mathrm{\AA}^{-1}$, which are the experimental values published in [1]. The mean magnetisation ϕ_0 was measured as well. Putting all these values into the generalised Brazovskii equations allows us to fit the theory to the experiments with the fit parameter u. To realise this, a further approximation is necessary. The function D, which is defined in equation (2.19), is approximated by the part containing the leading singularity D_{sing}. It is given by (cf. [1])

$$D_{\mathrm{sing}}\left(\kappa_\perp^2, \kappa_\parallel^2\right) = \frac{Q^3 k_B T}{\sqrt{2}\pi} \sqrt{\kappa_\perp^2 + \kappa_\parallel^2}\, \mathcal{Y}\left(\frac{\kappa_\perp^2 - \kappa_\parallel^2}{\kappa_\perp^2 + \kappa_\parallel^2}\right) \tag{4.10}$$

with

$$\mathcal{Y}(\alpha) = \sqrt{1+\alpha} - \frac{1}{\pi} \int_{-\infty}^{\infty} ds \left(1 - \sqrt{\frac{1+s^2}{\alpha}}\, \arctan \sqrt{\frac{\alpha}{1+s^2}}\right). \tag{4.11}$$

The fit was done by hand since it was already difficult to solely solve the self-consistency equations numerically. Therefore, it was not possible to do a numerical fit to the data without bigger efforts. Figure 13 shows the experimental data (dots) in comparison to the fit (line) for different magnetic fields as a function of temperature. $\kappa_\parallel$ is always plotted in red while $\kappa_\perp$ is plotted in yellow. At zero magnetic field both are equal. $\kappa_\perp = \kappa_\parallel = \kappa$ is then plotted in orange.

One can see that the theory works quite well for small external magnetic fields. However, it breaks down at a significant increase of the magnetic field. The best fit was obtained for a value of $u \approx 0.25\,\mathrm{meV/\AA}^3$, which agrees approximately with the experimental value given in [1] of $u \approx 0.32\,\mathrm{meV/\AA}^3$.

For the higher fields $\kappa_\perp$ becomes zero at some point. This would correspond to a second order phase transition. However, the phase transition between the fluctuation-disordered regime and the conical or the skyrmion phase is of first order. The exact position of the first order phase transition predicted by the theory is not yet calculated for finite fields. For $B = 0\,\mathrm{mT}$ theory predicts a slightly higher critical temperature than the experimental value of 29 K, namely $T_c \simeq 29.3\,\mathrm{K}$. However, theory predicts a first order transition for all values of the magnetic field

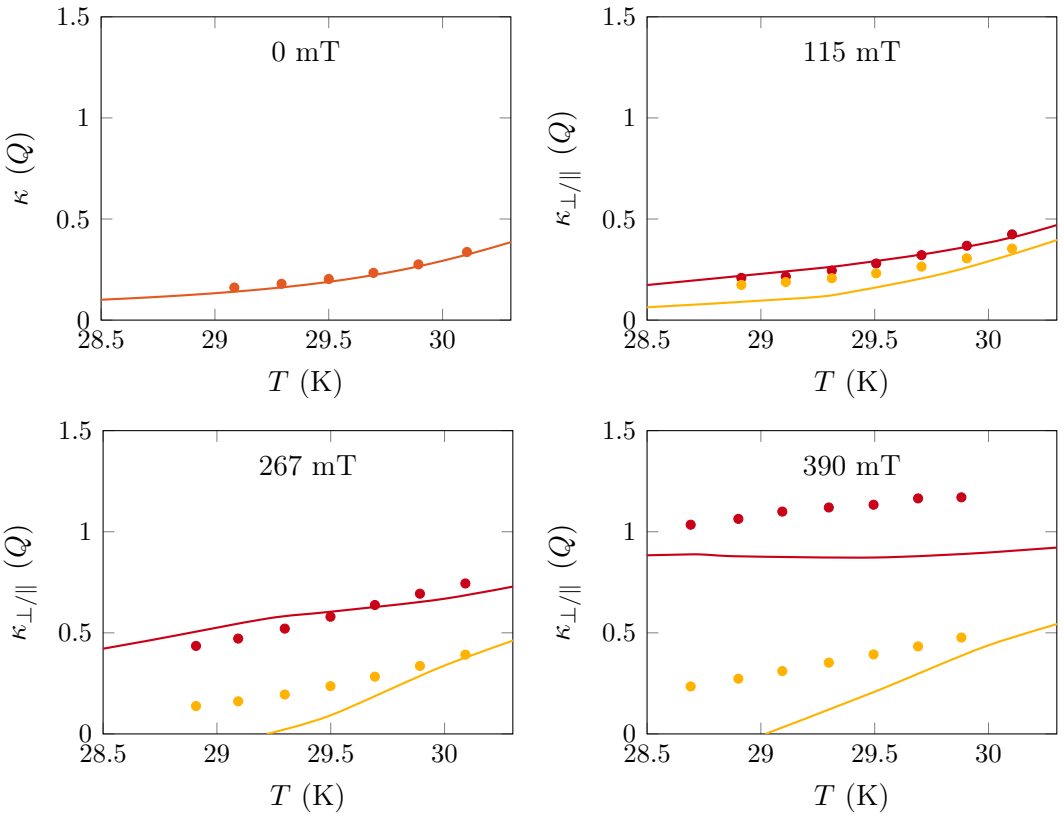

Figure 13: Neutron scattering data provided by J. Kindervater (dots) for $\kappa_\perp$ (yellow) and $\kappa_\parallel$ (red) in comparison to the generalised Brazovskii equations (lines) for different magnetic fields [20].

and temperature [8]. This is not the case. The experimental phase diagram in figure 1 shows that there exists a tricritical point at which the transition becomes second order again. In this phase space region one has to include all diagrams and cannot calculate self-consistently anymore. It is not sufficient to make the Hartree-Fock-Brazovskii approximation. The predicted first order transition is an artefact of this theory which is not applicable in this region of the phase diagram.

The calculated $\kappa_{\perp/\parallel}$ only exist in the fluctuation-disordered regime. If the transition temperature of the first order transition predicted by the theory lies above the temperature for which $\kappa_\perp$ vanishes, then the first order transition happens first and the second order transition does not appear. On the other hand, if the first order transition temperature lies below the value where $\kappa_\perp$ becomes zero, one may assume that this is a numerical problem since a first order transition is observed below the tricritical point in the experiments [1, 21].

390 mT is close to the tricritcal point where the theory looses validity. Therefore, the deviation between the experimental and theoretical values of $\kappa_\perp$ and $\kappa_\parallel$ is large. The splitting between $\kappa_\parallel$ and $\kappa_\perp$ is still predicted but the quantitative correspondence becomes worse.

4.3. Dynamical case

Eventually, we can switch on dynamics, i. e. choose $\Omega \neq 0$. Then we must use the full inverse Green's function as written down in equation (5.1).

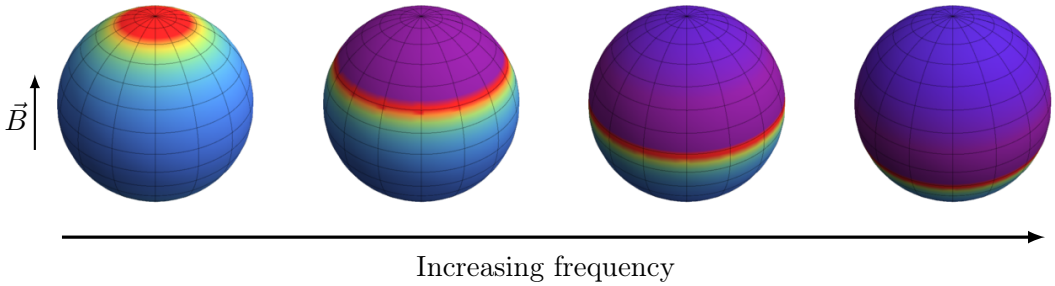

Figure 14: Tr $G(\vec{q})$ with $|\vec{q}| = 1$ for increasing frequency at a constant (finite) magnetic field

We choose a constant magnetic field pointing in z-direction and increase the frequency. Again, we examine $\mathrm{Tr}\, G$ on the sphere in momentum space with radius Q. This is shown in figure 14.

We observe that the divergence moves across the sphere from the north pole to the south pole when increasing the frequency from the left ($\Omega = 0$) to the right sphere. Finally, the divergence vanishes and the sphere remains without any divergences for higher frequencies.

5. Self-energy for interacting magnons

The dimensionless Green's function of the theory reads

$$G^{-1}(\vec{q},\Omega) = \begin{pmatrix} 1+q^2+\kappa_\perp^2 & -i\left(1+\kappa_\perp^2\right)(i\Omega) - 2iq_3 & 2iq_2 \\ i\left(1+\kappa_\perp^2\right)(i\Omega) + 2iq_3 & 1+q^2+\kappa_\perp^2 & -2iq_1 \\ -2iq_2 & 2iq_1 & 1+q^2+\kappa_\parallel^2 \end{pmatrix} . \tag{5.1}$$

As before, all momenta are measured in units of Q and the frequency Ω is measured in units of the electron-spin resonance frequency $\omega_{\text{ferro}} = \frac{g\mu_B B}{\hbar}$. To arrive at a form in correct units, one has to multiply G^{-1} with JQ^2. The calculation in the following will be done in the dimensionless form.

First we consider the spectrum, i. e. the eigenenergies of the correlation function. These are obtained by solving $\det G^{-1} = 0$ for Ω. Since we have neglected the damping term in the (3,3)-element, we have two energies, namely

$$\epsilon_\pm(\vec{q}) = \frac{1}{1+\kappa_\perp^2}\left(-2q_3 \pm \sqrt{\left(1+q^2+\kappa_\perp^2\right)^2 - 4\left(q_1^2+q_2^2\right)\frac{1+q^2+\kappa_\perp}{1+q^2+\kappa_\parallel}}\right) . \tag{5.2}$$

We use the short hand notation $|\vec{q}| \equiv q$. These two dispersion relations are connected to each other by the symmetry $\epsilon_+(\vec{q}) = -\epsilon_-(-\vec{q})$. $\epsilon_+(\vec{q})$ is positive for all momenta $\vec{q}$, i. e. $\epsilon_+(\vec{q}) > 0$.

The energy $\epsilon_+(\vec{q})$ has a minimum for $\vec{q}$ pointing in z-direction at $q_3 = 1$, namely

$$\epsilon_+(\vec{q} = \hat{e}_3) \equiv \epsilon_{\min} = \frac{\kappa_\perp^2}{1+\kappa_\perp^2} . \tag{5.3}$$

For $\vec{q}$ lying within the equatorial plane, i. e. $q_3 = 0$, there is a local minimum which is slightly shifted away from $q = 1$. The value of this minimum is bigger than the minimum in z-direction, and it does not have such a nice analytical form. Therefore, $\epsilon_+(\hat{e}_3) = \epsilon_{\min}$ is a global minimum. Figure 15 shows ϵ_+ as a function of $\vec{q}$ with different parametrisations of the momentum.

Since the Green's function is the two point function of two real bosonic fields, namely the magnetisation, it is real in position and time space.

$$G_{ij}(\vec{x},t) = \left\langle \phi_i(0,0)\phi_j(\vec{x},t)\right\rangle \tag{5.4}$$

Fourier transforming this object leads to

$$G_{ij}(\vec{q},\omega) = \int dt\, d^3x\, \Theta(t)\left\langle \phi_i(0,0)\phi_j(\vec{x},t)\right\rangle e^{i\omega t - i\vec{q}\cdot\vec{x}} . \tag{5.5}$$

From this, it is obvious that $G_{ij}(\vec{q},\omega) = G_{ji}(-\vec{q},-\omega)^*$. Therefore, the imaginary part of the diagonal elements of the Green's function has to be odd under the transformation $(\vec{q},\omega) \to (-\vec{q},-\omega)$, and the real part is even.

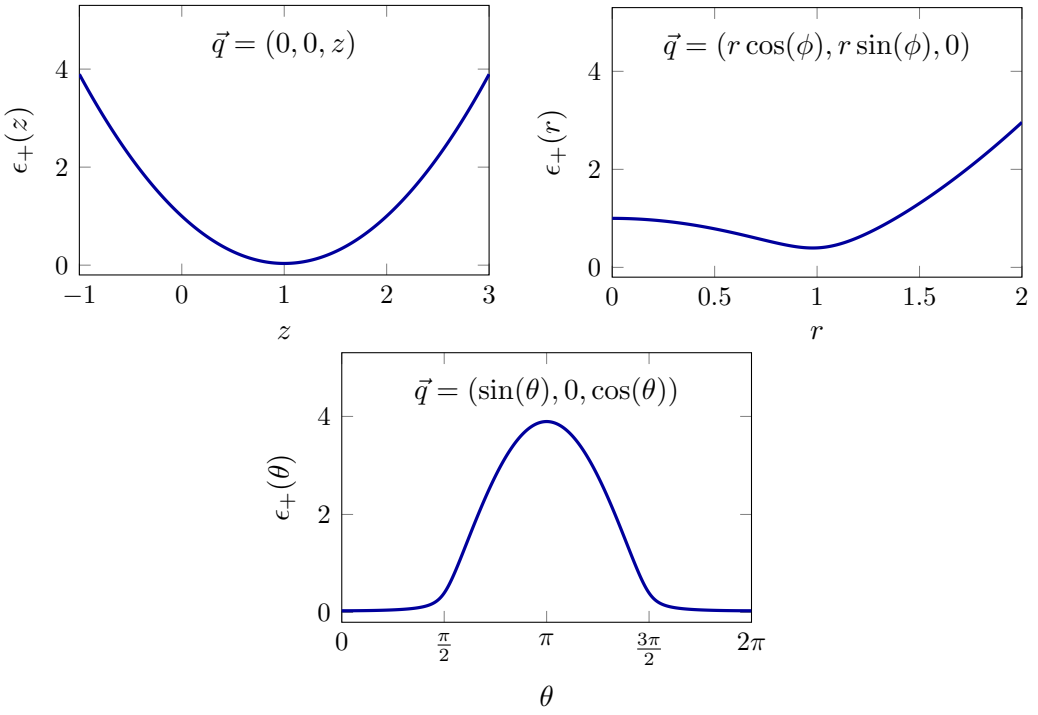

Figure 15: $\epsilon_+(\vec{q})$ for different parametrisations of $\vec{q}$ with $(\kappa_\parallel, \kappa_\perp) = (0.22, 0.19)$. In the second plot ϕ is arbitrary.

To explicitly write down the Green's function, we have to invert equation (5.1). We can write it in the following form by doing a partial fraction decomposition:

$$G(\vec{q}, \Omega) = \frac{a_+(\vec{q})}{i\Omega - \epsilon_+(\vec{q})} + \frac{a_-(\vec{q})}{i\Omega - \epsilon_-(\vec{q})} + b(\vec{q}) \,, \tag{5.6}$$

where

$$\begin{aligned} a_\pm(\vec{q})_{ij} = \mp \Big[\left(1 + \kappa_\perp^2\right)^2 \left(1 + q^2 + \kappa_\parallel^2\right) \left(\epsilon_+(\vec{q}) - \epsilon_-(\vec{q})\right) \Big]^{-1} \Big[& 2i\varepsilon_{ij3} q_3 \left(1 + q^2 + \kappa_\parallel^2\right) \\ & + 2i\varepsilon_{ijn} (q_\perp)_n \left(1 + q^2 + \kappa_\perp^2\right) + i\varepsilon_{ij3} \left(1 + q^2 + \kappa_\parallel^2\right) \left(1 + \kappa_\perp^2\right) \epsilon_\pm(\vec{q}) \\ & - 2 \left(1 + \kappa_\perp^2\right) \epsilon_\pm(\vec{q}) \left(q_i \delta_{j3} + q_j \delta_{i3}\right) + \left(\delta_{ij} - \delta_{i3}\delta_{j3}\right) \left(1 + q^2 + \kappa_\perp^2\right) \left(1 + q^2 + \kappa_\parallel^2\right) \\ & + \delta_{i3}\delta_{j3} \left(\left(1 + q^2 + \kappa_\perp^2\right)^2 - \left(1 + \kappa_\perp^2\right)^2 \epsilon_\pm^2(\vec{q}) \right) - 4 q_i q_j \Big] \end{aligned} \tag{5.7}$$

and

$$b(\vec{q}) = -\,\delta_{i3}\,\delta_{j3}\,\frac{1}{1 + q^2 + \kappa_\parallel^2} \,. \tag{5.8}$$

The momentum component perpendicular to the external magnetic field is given by $q_\perp = \vec{q} - \hat{n}(\vec{q} \cdot \vec{n}) = (q_1, q_2, 0)^T$ for $\vec{B} = B\hat{n} = B\hat{e}_3$. One can show that $a_+(\vec{q}) = -a_-^*(-\vec{q})$. Using the symmetries of the energies discussed above and of

the matrices $a_\pm$, we can rewrite the Green's function in the following form.

$$G(\vec{q},\Omega) = \frac{a_+(\vec{q})}{i\Omega - \epsilon_+(\vec{q})} - \frac{a_+^*(-\vec{q})}{i\Omega + \epsilon_+(-\vec{q})} + b(\vec{q}) \; . \tag{5.9}$$

Therefore, there is only one dispersion $\epsilon_+(\vec{q}) \equiv \epsilon(\vec{q})$ and one spectral function $a_+(\vec{q}) \equiv a(\vec{q})$ left to compute. The Green's function then reads

$$G(\vec{q},\Omega) = \frac{a(\vec{q})}{i\Omega - \epsilon(\vec{q})} - \frac{a^*(-\vec{q})}{i\Omega + \epsilon(-\vec{q})} + b(\vec{q}) \; . \tag{5.10}$$

In the following, we will neglect the third term, i. e. $b(\vec{q})$, since it does not include any dynamics.

In the end, what we want to calculate is the susceptibility χ, for which

$$\chi^{-1} = \chi_0^{-1} - \Pi \; . \tag{5.11}$$

holds. Π is the self-energy and has to be calculated first. We will do perturbation theory up to second order. The diagrammatic representation is shown in (5.12). The first term is of first order, and it is called the Hartree-Fock term. It is already included in the Brazovskii theory but does not contain any dynamics. Thus, the second order terms gives the first contribution to $\Pi(\vec{q},\Omega)$ at a finite frequency Ω.

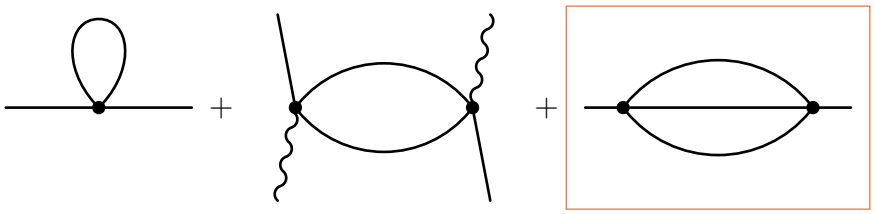

(5.12)

A further diagram, which is not considered here, results when we, again, do perturbation theory up to second order but then couple two fields to the mean-field, i. e. the mean magnetisation, one at each vertex. The mean magnetisation is denoted by a wiggly line. This is the second diagram in the diagrammatic equation (5.12). In the whole calculation we are only considering the case $\vec{q} = 0$, and we are looking for fluctuations composed of triangles. This self-energy diagram consists only of two Green's function. No triangular structure can thus be observed. Furthermore, since it includes two mean magnetisations, it comes with a factor M_0^2. For small magnetic fields this will be suppressed. However, the corresponding free-energy diagram would already include triangles.

We will, therefore, restrict ourselves to the third diagram, the one in the box.

To calculate the self-energy, we make use of Wick's theorem and arrive at the

following expression:

$$\begin{aligned}\Pi(\vec{q},\Omega)_{ij} =& 2\sum_{\vec{q}_1,\vec{q}_2,\vec{q}_3}\sum_{\omega_1,\omega_2,\omega_3}\sum_{k,l=1}^{3}\delta_{\vec{q}_1+\vec{q}_2+\vec{q}_3,\vec{q}}\,\delta_{\omega_1+\omega_2+\omega_3,\Omega}\\ &\cdot\Big[G_{ij}(\vec{q}_1,\omega_1)G_{kl}(\vec{q}_2,\omega_2)G_{kl}(\vec{q}_3,\omega_3)+G_{kj}(\vec{q}_1,\omega_1)G_{il}(\vec{q}_2,\omega_2)G_{kl}(\vec{q}_3,\omega_3)\\ &+G_{lj}(\vec{q}_1,\omega_1)G_{ik}(\vec{q}_2,\omega_2)G_{lk}(\vec{q}_3,\omega_3)\Big] \qquad (5.13)\\ =& 2\sum_{q_1,q_2,q_3}\sum_{\omega_1,\omega_2,\omega_3}\Big[G(\vec{q}_1,\omega_1)_{ij}\mathrm{Tr}\left(G(\vec{q}_2,\omega_2)G(\vec{q}_3,\omega_3)^T\right)\\ &+2\left(G(\vec{q}_2,\omega_2)G(\vec{q}_3,\omega_3)^TG(\vec{q}_1,\omega_1)\right)_{ij}\Big]\cdot\delta_{\vec{q}_1+\vec{q}_2+\vec{q}_3,\vec{q}}\,\delta_{\omega_1+\omega_2+\omega_3,\Omega}\,. \qquad (5.14)\end{aligned}$$

Now we can put in the expression for the Green's function derived above. We will neglect the $b(\vec{q})$-term as mentioned. Furthermore, we can integrate out the bosonic Matsubara frequencies ω_1, ω_2 and ω_3.

$$\begin{aligned}\Pi(\vec{q},\Omega) =& 2\sum_{\vec{q}_1,\vec{q}_2,\vec{q}_3}\sum_{\sigma_1,\sigma_2,\sigma_3=\pm}\frac{A_{\sigma_1,\sigma_2,\sigma_3}(\vec{q}_1,\vec{q}_2,\vec{q}_3)}{i\Omega-\epsilon_{\sigma_1}(\vec{q}_1)-\epsilon_{\sigma_2}(\vec{q}_2)-\epsilon_{\sigma_3}(\vec{q}_3)}\,\delta_{\vec{q}_1+\vec{q}_2+\vec{q}_3,\vec{q}}\\ &\cdot\left[n(\epsilon_{\sigma_1}(\vec{q}_1))-n(-\epsilon_{\sigma_2}(\vec{q}_2)-\epsilon_{\sigma_3}(\vec{q}_3))\right]\left[n(\epsilon_{\sigma_2}(\vec{q}_2))-n(-\epsilon_{\sigma_3}(\vec{q}_3))\right], \qquad (5.15)\end{aligned}$$

where $A_{\sigma_1,\sigma_2,\sigma_3}(\vec{q}_1,\vec{q}_2,\vec{q}_3)$ is a short hand notation for the matrix part, namely

$$A_{\sigma_1,\sigma_2,\sigma_3}(\vec{q}_1,\vec{q}_2,\vec{q}_3) := a_{\sigma_1}(\vec{q}_1)\,\mathrm{Tr}\left[a_{\sigma_2}(\vec{q}_2)a_{\sigma_3}(\vec{q}_3)^T\right]+2\,a_{\sigma_2}(\vec{q}_2)\,a_{\sigma_3}(\vec{q}_3)^Ta_{\sigma_1}(\vec{q}_1)\,. \qquad (5.16)$$

$n(\epsilon) = (e^{\beta\epsilon}-1)^{-1}$ is the Bose function with $\beta = \hbar\omega_{\mathrm{ferro}}/(k_BT)$ since we are measuring the frequencies in units of the ferromagnetic resonance frequency. The symmetries of the matrices $a_\sigma(\vec{q})$, $a_\sigma(\vec{q}) = -a^*_{-\sigma}(-\vec{q})$, lead to the symmetry of $A_{\sigma_1,\sigma_2,\sigma_3}(\vec{q}_1,\vec{q}_2,\vec{q}_3)$, $A_{\sigma_1,\sigma_2,\sigma_3}(\vec{q}_1,\vec{q}_2,\vec{q}_3) = -A^*_{-\sigma_1,-\sigma_2,-\sigma_3}(-\vec{q}_1,-\vec{q}_2,-\vec{q}_3)$.
Since we are looking at experiments with a homogeneous magnetic field, we will only consider the case of $\vec{q}=0$. In order to investigate the processes which take place, we use the properties of the Bose function and rewrite equation (5.15).

$$\begin{aligned}\Pi(0,\Omega) =& 2\sum_{\vec{q}_1,\vec{q}_2,\vec{q}_3}\sum_{\sigma_1,\sigma_2,\sigma_3=\pm}\frac{A_{\sigma_1,\sigma_2,\sigma_3}(\vec{q}_1,\vec{q}_2,\vec{q}_3)}{i\Omega-\sigma_1\epsilon(\sigma_1\vec{q}_1)-\sigma_2\epsilon(\sigma_2\vec{q}_2)-\sigma_3\epsilon(\sigma_3\vec{q}_3)}\,\delta_{\vec{q}_1+\vec{q}_2+\vec{q}_3,0}\\ &\cdot\Big[\left(1+n(\sigma_1\epsilon(\sigma_1\vec{q}_1))\right)\left(1+n(\sigma_2\epsilon(\sigma_2\vec{q}_2))\right)\left(1+n(\sigma_3\epsilon(\sigma_3\vec{q}_3))\right)\\ &-n(\sigma_1\epsilon(\sigma_1\vec{q}_1))n(\sigma_2\epsilon(\sigma_2\vec{q}_2))n(\sigma_3\epsilon(\sigma_3\vec{q}_3))\Big] \qquad (5.17)\end{aligned}$$

Using all the symmetries collected for ϵ and A and the property of the Bose function

$n(-\epsilon) = -(1 + n(\epsilon))$, we can rewrite this:

$$\begin{aligned}\Pi(0,\Omega) = &-2\sum_{\vec{q}_1,\vec{q}_2,\vec{q}_3}\sum_{\sigma_1,\sigma_2,\sigma_3=\pm} n(\sigma_1\epsilon(\sigma_1\vec{q}_1))\, n(\sigma_2\epsilon(\sigma_2\vec{q}_2))\, n(\sigma_3\epsilon(\sigma_3\vec{q}_3))\, \delta_{\vec{q}_1+\vec{q}_2+\vec{q}_3,0} \\ &\cdot\left[\frac{A_{\sigma_1,\sigma_2,\sigma_3}(\vec{q}_1,\vec{q}_2,\vec{q}_3)}{i\Omega - \sigma_1\epsilon(\sigma_1\vec{q}_1) - \sigma_2\epsilon(\sigma_2\vec{q}_2) - \sigma_3\epsilon(\sigma_3\vec{q}_3)}\right. \\ &\left.- \frac{A^*_{\sigma_1,\sigma_2,\sigma_3}(\vec{q}_1,\vec{q}_2,\vec{q}_3)}{i\Omega + \sigma_1\epsilon(\sigma_1\vec{q}_1) + \sigma_2\epsilon(\sigma_2\vec{q}_2) + \sigma_3\epsilon(\sigma_3\vec{q}_3)}\right]. \end{aligned} \tag{5.18}$$

There are four processes possible: Three magnons can be absorbed ($\sigma_1 = \sigma_2 = \sigma_3 = +1$) or emitted ($\sigma_1 = \sigma_2 = \sigma_3 = -1$), or two can be absorbed and one emitted (two $\sigma_i = +1$, one $\sigma_i = -1$) or vice versa, i. e. two emitted and one absorbed (two $\sigma_i = -1$, one $\sigma_i = +1$), depending on the signs σ_i.

Since $\beta\epsilon$ is small in the regime we are interested in, we can expand three the Bose functions up to order $\mathcal{O}(\frac{1}{\beta^2})$ and approximate $n(\epsilon) \simeq (\beta\epsilon)^{-1} - \frac{1}{2}$. Since the term of order β^{-3} vanishes due to the symmetry of expression (5.18), the first contributing order is β^{-2}. The self-energy then reads

$$\begin{aligned}\Pi(0,\Omega) =&2\beta^{-2}\sum_{\vec{q}_1,\vec{q}_2,\vec{q}_3}\sum_{\sigma_1,\sigma_2,\sigma_3=\pm} \frac{\sigma_1\epsilon(\sigma_1\vec{q}_1) + \sigma_2\epsilon(\sigma_1\vec{q}_2) + \sigma_3\epsilon(\sigma_1\vec{q}_3)}{2\sigma_1\epsilon(\sigma_1\vec{q}_1)\ \sigma_2\epsilon(\sigma_2\vec{q}_2)\ \sigma_3\epsilon(\sigma_3\vec{q}_3)}\, \delta_{\vec{q}_1+\vec{q}_2+\vec{q}_3,0} \\ &\cdot\left[\frac{A_{\sigma_1,\sigma_2,\sigma_3}(\vec{q}_1,\vec{q}_2,\vec{q}_3)}{i\Omega - \sigma_1\epsilon(\sigma_1\vec{q}_1) - \sigma_2\epsilon(\sigma_2\vec{q}_2) - \sigma_3\epsilon(\sigma_3\vec{q}_3)}\right. \\ &\left.- \frac{A^*_{\sigma_1,\sigma_2,\sigma_3}(\vec{q}_1,\vec{q}_2,\vec{q}_3)}{i\Omega + \sigma_1\epsilon(\sigma_1\vec{q}_1) + \sigma_2\epsilon(\sigma_2\vec{q}_2) + \sigma_3\epsilon(\sigma_3\vec{q}_3)}\right]. \end{aligned} \tag{5.19}$$

First, we want to consider the imaginary part of the self-energy. We do an analytically continuation of the frequency $i\Omega \to \Omega + i0^+$ since we are only interested in the retarded part. When taking the imaginary part, one obtains two terms. One is proportional to $\operatorname{Im} A_{\sigma_1,\sigma_2,\sigma_3}(\vec{q}_1,\vec{q}_2,\vec{q}_3)$ and one proportional to $\operatorname{Re} A_{\sigma_1,\sigma_2,\sigma_3}(\vec{q}_1,\vec{q}_2,\vec{q}_3)$. It turns out that the former one vanishes when taking out the momentum integrations for the diagonal elements. Thus, it is sufficient to only consider the latter term when calculating the diagonal elements.

$$\begin{aligned}\operatorname{Im}\Pi_{\text{diag}}(0,\Omega) = &-\beta^{-2}\pi\sum_{\vec{q}_1,\vec{q}_2,\vec{q}_3}\sum_{\sigma_1,\sigma_2,\sigma_3=\pm} \frac{\sigma_1\epsilon(\sigma_1\vec{q}_1) + \sigma_2\epsilon(\sigma_1\vec{q}_2) + \sigma_3\epsilon(\sigma_1\vec{q}_3)}{\sigma_1\epsilon(\sigma_1\vec{q}_1)\ \sigma_2\epsilon(\sigma_2\vec{q}_2)\ \sigma_3\epsilon(\sigma_3\vec{q}_3)}\, \delta_{\vec{q}_1+\vec{q}_2+\vec{q}_3,0} \\ &\cdot\Big[\delta\big(\Omega - \sigma_1\epsilon(\sigma_1\vec{q}_1) - \sigma_2\epsilon(\sigma_2\vec{q}_2) - \sigma_3\epsilon(\sigma_3\vec{q}_3)\big)\Big. \\ &\Big.- \delta\big(\Omega + \sigma_1\epsilon(\sigma_1\vec{q}_1) + \sigma_2\epsilon(\sigma_2\vec{q}_2) + \sigma_3\epsilon(\sigma_3\vec{q}_3)\big)\Big]\operatorname{Re} A_{\sigma_1,\sigma_2,\sigma_3}(\vec{q}_1,\vec{q}_2,\vec{q}_3). \end{aligned} \tag{5.20}$$

This contains an integral over three three dimensional momenta. Their number is reduced by three due to the condition that they have to sum up to zero, i. e. that they build a triangle due to momentum conservation. The integration dimensions

are additionally scaled down by one due to the delta functions. In the end we are left with a five dimensional integral, which we will investigate numerically via Monte Carlo integration in the next section.

For the off-diagonal elements, however, the story is different. The part proportional to $\mathrm{Re}\, A_{\sigma_1,\sigma_2,\sigma_3}(\vec{q}_1,\vec{q}_2,\vec{q}_3)$ vanishes for all off-diagonal elements. The one proportional to $\mathrm{Im}\, A_{\sigma_1,\sigma_2,\sigma_3}(\vec{q}_1,\vec{q}_2,\vec{q}_3)$ does not, at least for the (1,2)- and the (2,1)-element. The other off-diagonal elements vanish in both cases.

To calculate the (1,2)-element numerically via the Monte Carlo method, we apply a little trick to avoid numerical troubles caused by the divergence in the denominator. This component of the imaginary part of the self-energy reads

$$\begin{aligned}\mathrm{Im}\,\Pi_{\text{off-diag}}(0,\Omega) = \beta^{-2} \sum_{\vec{q}_1,\vec{q}_2,\vec{q}_3} \sum_{\sigma_1,\sigma_2,\sigma_3=\pm} & \frac{\sigma_1\epsilon(\sigma_1\vec{q}_1)+\sigma_2\epsilon(\sigma_1\vec{q}_2)+\sigma_3\epsilon(\sigma_1\vec{q}_3)}{\sigma_1\epsilon(\sigma_1\vec{q}_1)\;\sigma_2\epsilon(\sigma_2\vec{q}_2)\;\sigma_3\epsilon(\sigma_3\vec{q}_3)}\;\delta_{\vec{q}_1+\vec{q}_2+\vec{q}_3,0} \\ \cdot\,\mathrm{Im}\, A_{\sigma_1,\sigma_2,\sigma_3}(\vec{q}_1,\vec{q}_2,\vec{q}_3) \cdot \mathcal{P}\Bigg[& \frac{1}{\Omega-\sigma_1\epsilon(\sigma_1\vec{q}_1)-\sigma_2\epsilon(\sigma_2\vec{q}_2)-\sigma_3\epsilon(\sigma_3\vec{q}_3)} \\ + & \frac{1}{\Omega+\sigma_1\epsilon(\sigma_1\vec{q}_1)+\sigma_2\epsilon(\sigma_2\vec{q}_2)+\sigma_3\epsilon(\sigma_3\vec{q}_3)}\Bigg]. \end{aligned} \tag{5.21}$$

$\mathcal{P}$ denotes the principle value integral. We multiply this by unity, which is represented by an integral over a delta function,

$$1 = \int d\omega\, \delta\big(\omega-\sigma_1\epsilon(\sigma_1\vec{q}_1)-\sigma_2\epsilon(\sigma_2\vec{q}_2)-\sigma_3\epsilon(\sigma_3\vec{q}_3)\big)\,. \tag{5.22}$$

We can exchange now the sums with the integral over ω. This allows to rewrite equation (5.21) as

$$\begin{aligned}\mathrm{Im}\,\Pi_{\text{off-diag}}(0,\Omega) = \beta^{-2} \int d\omega \sum_{\vec{q}_1,\vec{q}_2,\vec{q}_3} \sum_{\sigma_1,\sigma_2,\sigma_3=\pm} & \Bigg[\frac{\mathrm{Im}\, A_{\sigma_1,\sigma_2,\sigma_3}(\vec{q}_1,\vec{q}_2,\vec{q}_3)}{\sigma_1\epsilon(\sigma_1\vec{q}_1)\;\sigma_2\epsilon(\sigma_2\vec{q}_2)\;\sigma_3\epsilon(\sigma_3\vec{q}_3)} \\ \cdot\,\mathcal{P}\frac{2\,\Omega\,\omega}{\Omega^2-\omega^2}\,\delta\Big(\omega-\sigma_1\epsilon(\sigma_1\vec{q}_1)-\sigma_2\epsilon(\sigma_2\vec{q}_2)-\sigma_3\epsilon(\sigma_3\vec{q}_3)\Big)\Bigg]\,. \end{aligned} \tag{5.23}$$

Numerically, we will only calculate the following object which has the same structure as the integral of the diagonal elements (5.20):

$$\begin{aligned}\nu(\omega) = \beta^{-2} \sum_{\vec{q}_1,\vec{q}_2,\vec{q}_3} \sum_{\sigma_1,\sigma_2,\sigma_3=\pm} & \Bigg[\frac{\mathrm{Im}\, A_{\sigma_1,\sigma_2,\sigma_3}(\vec{q}_1,\vec{q}_2,\vec{q}_3)}{\sigma_1\epsilon(\sigma_1\vec{q}_1)\;\sigma_2\epsilon(\sigma_2\vec{q}_2)\;\sigma_3\epsilon(\sigma_3\vec{q}_3)} \\ \cdot\,\delta\Big(\omega-\sigma_1\epsilon(\sigma_1\vec{q}_1)-\sigma_2\epsilon(\sigma_2\vec{q}_2)-\sigma_3\epsilon(\sigma_3\vec{q}_3)\Big)\Bigg]\,. \end{aligned} \tag{5.24}$$

To calculate the imaginary part of the off-diagonal self-energy element, we integrate over ω and get

$$\mathrm{Im}\,\Pi_{\text{off-diag}}(0,\Omega) = \int d\omega\, \mathcal{P}\frac{\Omega\,\omega}{\Omega^2-\omega^2}\,\nu(\omega)\,. \tag{5.25}$$

The integration over ω is done analytically assuming that $\nu(\omega)$ is constant in the intervals which are chosen as step sizes in the numerical part.

Furthermore, it is possible to calculate the real part of the off-diagonal element just like the imaginary part of the diagonal element and the real part of the diagonal element like the imaginary part of the off-diagonal element.

The real part of the off-diagonal element reads analogously to equation (5.20)

$$\begin{aligned}\mathrm{Re}\,\Pi_{\text{off-diag}}(0,\Omega) = \beta^{-2}\pi \sum_{\vec{q}_1,\vec{q}_2,\vec{q}_3} \sum_{\sigma_1,\sigma_2,\sigma_3=\pm} \frac{\sigma_1\epsilon(\sigma_1\vec{q}_1)+\sigma_2\epsilon(\sigma_1\vec{q}_2)+\sigma_3\epsilon(\sigma_1\vec{q}_3)}{\sigma_1\epsilon(\sigma_1\vec{q}_1)\;\sigma_2\epsilon(\sigma_2\vec{q}_2)\;\sigma_3\epsilon(\sigma_3\vec{q}_3)}\delta_{\vec{q}_1+\vec{q}_2+\vec{q}_3,0} \\ \cdot \mathrm{Im}\,A_{\sigma_1,\sigma_2,\sigma_3}(\vec{q}_1,\vec{q}_2,\vec{q}_3)\Big[\delta\big(\Omega-\sigma_1\epsilon(\sigma_1\vec{q}_1)-\sigma_2\epsilon(\sigma_2\vec{q}_2)-\sigma_3\epsilon(\sigma_3\vec{q}_3)\big) \\ +\delta\big(\Omega+\sigma_1\epsilon(\sigma_1\vec{q}_1)+\sigma_2\epsilon(\sigma_2\vec{q}_2)+\sigma_3\epsilon(\sigma_3\vec{q}_3)\big)\Big]\,. \qquad (5.26)\end{aligned}$$

Correspondingly, we can calculate the real part of the diagonal element just like the imaginary part of the off-diagonal element:

$$\begin{aligned}\mathrm{Re}\,\Pi_{\text{diag}}(\Omega) =& \beta^{-2}\int d\omega\,\mathcal{P}\frac{2\,\omega^2}{\Omega^2-\omega^2}\sum_{\vec{q}_1,\vec{q}_2,\vec{q}_3}\sum_{\sigma_1,\sigma_2,\sigma_3=\pm}\frac{\mathrm{Re}\,A_{\sigma_1,\sigma_2,\sigma_3}(\vec{q}_1,\vec{q}_2,\vec{q}_3)}{\sigma_1\epsilon(\sigma_1\vec{q}_1)\;\sigma_2\epsilon(\sigma_2\vec{q}_2)\;\sigma_3\epsilon(\sigma_3\vec{q}_3)} \\ &\cdot\delta\big(\omega-\sigma_1\epsilon(\vec{q}_1)-\sigma_2\epsilon(\vec{q}_2)-\sigma_3\epsilon(\vec{q}_3)\big)\;\delta_{\vec{q}_1+\vec{q}_2+\vec{q}_3,0}\;. \qquad (5.27)\end{aligned}$$

It is possible to show that the Kramers-Kronig relation of (5.20) [22],

$$\mathrm{Re}\,\Pi_{\text{diag}}(0,\omega) = \frac{1}{\pi}\int d\Omega\;\mathrm{Im}\,\Pi_{\text{diag}}(0,\Omega)\,\mathcal{P}\frac{1}{\Omega-\omega}\;, \qquad (5.28)$$

leads to the same form for the real part of the diagonal element. Analogously, this holds for the correspondence between the real and imaginary parts of the off-diagonal elements.

6. Numerical evaluation of the self-energy

To perform the numerical integration, the matrix elements, over which we would like to integrate, were exported from Mathematica into a C++ program. To solve the integral numerically, we use the Monte Carlo method, which is described in Appendix C. The code for the Monte Carlo integration is taken from [23].

The integration was done for each matrix element separately. It can be observed that the (1,1)-element and the (2,2)-element show exactly the same behaviour as expected for a system that is isotropic in these two directions. The (3,3)-element looks slightly different. The (1,3)-, (2,3)-, (3,1)- and (3,2)-element turn out to be zero and are, therefore, not considered further.

All results presented in this section are shown in a dimensionless form. For that reason, the self-energy was multiplied by a factor of JQ^2/u^2. In the next section the factors will be discussed in more detail.

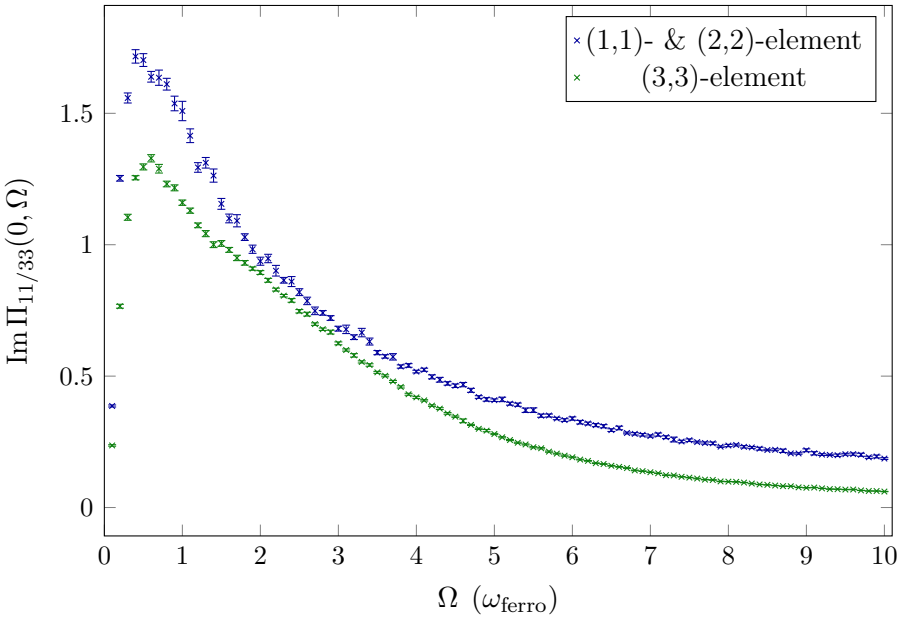

Figure 16: Diagonal elements of the self-enegy for $(\kappa_\parallel, \kappa_\perp) = (0.22, 0.19)$

Figure 16 shows exemplarily the result of the integration for the imaginary part of the diagonal elements. We observe one maximum at $\Omega \simeq 0.6$. However, this is not a sharp peak but has a finite width. On that account its origin cannot be a singularity remaining after the integration over all dimensions.

In the following, we will discuss where this maximum has its origin, i. e. which momentum triangles contribute most to the peak and which processes are dominant. Therefore, the phase space over which the integration is performed was restricted, e. g. by restricting the angles and the lengths of two of the momentum vectors. Since the third momentum vector is determined by the other two due to $\delta_{\vec{q}_1+\vec{q}_2+\vec{q}_3,0}$, it is sufficient to consider the configuration of two momentum vectors.

6.1. Equilateral triangles in the equatorial plane

To investigate if skyrmion type fluctuations give rise to the resonance behaviour in the fluctuation-disordered regime, we can integrate solely over equilateral triangles in the equatorial plane. This means we reduce the five dimensional integral to two dimensions, one absolute angle and the radius. For numerical reasons, we effectively integrated over a thin disk instead of a real plane.

The crosses in figure 17 show the result of the numerical integration. We observe a divergence at $\Omega = 0.4$, which corresponds to the minimal energy for the momentum vector lying in the equatorial plane.

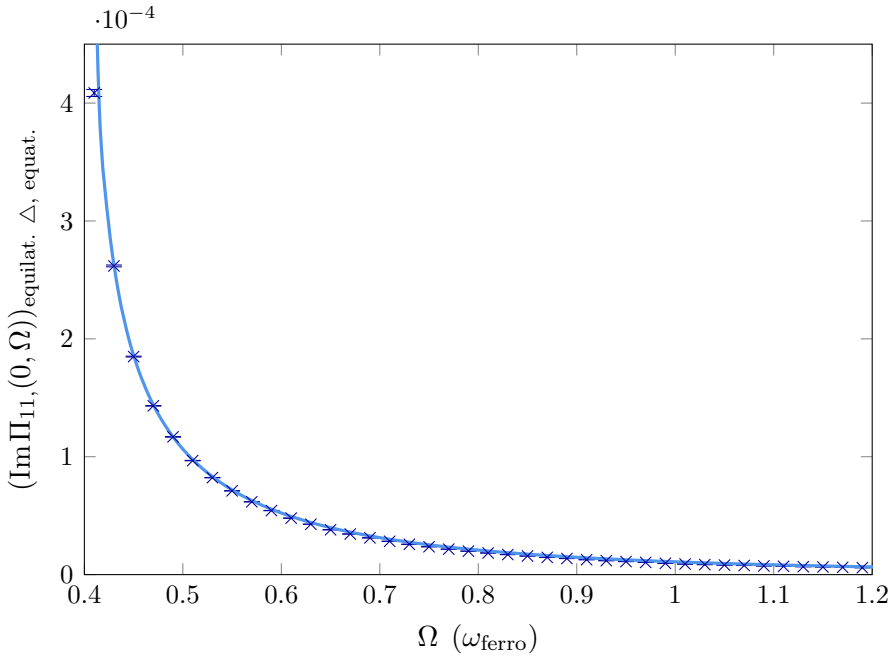

Figure 17: Integration over equilateral triangles in the equatorial plane. The crosses denote the result of the numerical integration, the line shows the analytically determined behaviour

However, this case can be solved analytically. Since the triangles all have the same length and lie in the equatorial plane, i. e. all z-components of the momenta vanish, the absolute values of the energies are equal, $|\epsilon_{\sigma_1}(\vec{q}_1)| = |\epsilon_{\sigma_2}(\vec{q}_2)| = |\epsilon_{\sigma_3}(\vec{q}_3)|$. The value of the energies only depends on the length of the momentum vectors as discussed in section 5. However, the signs can be different depending on the occurring process. According to equation (5.15) and with the Bose functions already expanded, the imaginary part of the self-energy is proportional to

$$\begin{aligned}\mathrm{Im}\,\Pi \propto{}& \delta\big(\Omega - \sigma_1\epsilon(\sigma_1\vec{q}_1) - \sigma_2\epsilon(\sigma_2\vec{q}_2) - \sigma_3\epsilon(\sigma_3\vec{q}_3)\big)\\ &\cdot\left[\frac{\sigma_1\epsilon(\sigma_1\vec{q}_1) + \sigma_2\epsilon(\sigma_2\vec{q}_2) + \sigma_3\epsilon(\sigma_3\vec{q}_3)}{\sigma_1\epsilon(\sigma_1\vec{q}_1)\,\sigma_2\epsilon(\sigma_2\vec{q}_2)\,\sigma_3\epsilon(\sigma_3\vec{q}_3)}\right].\end{aligned} \tag{6.1}$$

For $\Omega > 0$, there are only two processes possible, namely all $\sigma_i = +1$ or two $+1$

and one -1. We can thus rewrite the delta-function as $\delta(\Omega - \alpha\epsilon(r))$, where r is the length of the momentum vectors and $\alpha \in \{1, 3\}$. Using the delta-function reveals that the part from the Bose functions is proportional to $1/\Omega^2$ since $\Omega = \alpha\epsilon(r)$.

$$\operatorname{Im}\Pi \propto \frac{1}{\Omega^2}\,\delta\big(\Omega - \alpha\epsilon(r)\big) \tag{6.2}$$

There is a minimum for the energies as described in section 5, which is a lower limit for the frequency. We expand the energy around the minimum, which is slightly shifted away from Q. It is called $Q_{\min}$. Since this is a minimum, the first order is zero and we get

$$\operatorname{Im}\Pi \propto \frac{1}{\Omega^2}\,\delta\Big(\Omega - \alpha\,\epsilon(Q_{\min}) - \frac{\alpha}{2}\,\epsilon''(Q_{\min})\,(q - Q_{\min})^2\Big)\,. \tag{6.3}$$

We can rewrite the delta-function and arrive at

$$\begin{aligned}\operatorname{Im}\Pi &\propto \frac{1}{\Omega^2}\,\delta\big(q - Q_{\min}\big)\frac{1}{\sqrt{2|\epsilon''(Q_{\min})|\big(\Omega - \alpha\epsilon(Q_{\min})\big)}} \\ &\propto \frac{1}{\Omega^2\sqrt{\Omega - \alpha\epsilon(Q_{\min})}}\,\delta\big(q - Q_{\min}\big)\,.\end{aligned} \tag{6.4}$$

This means we observe two divergences, one for $\alpha = 1$ at $\Omega = \epsilon(Q_{\min})$ and one for $\alpha = 3$ at $\Omega = 3\epsilon(Q_{\min})$. However, as we will discuss in the next subsection, the processes with all signs being equal have a much lower weight than the processes with differing signs. Therefore, we only observe the first divergence with $\alpha = 1$. The line in figure 17 shows the analytically predicted behaviour with only the pre-factor calculated from one numerical value.

However, the position of this divergence does not correspond to the peak position observed in the calculation of the whole self-energy. Furthermore, by doing the integrations over the remaining three dimensions the divergence will be integrated out. The weight of the integral only over equilateral triangles in the equatorial plane is very small compared to the weight of the full integral. We can conclude that skyrmion type fluctuations do not have an extraordinary high contribution to the self-energy.

6.2. Different types of three-magnon processes

Four processes can take place depending on the different signs σ_1, σ_2 and σ_3. Physically, they correspond to the possibilities that three magnons can be absorbed or emitted and two can be absorbed and one emitted or one can be absorbed and two emitted. How much each of them contributes to the total integral can be examined by only integrating over the respective sum term of the sum over the σ_i.

Figure 18 shows these separate integrations. The upper left plot in 18 shows the two cases when all σ_i have the same sign. Both cases show exactly the same behaviour.

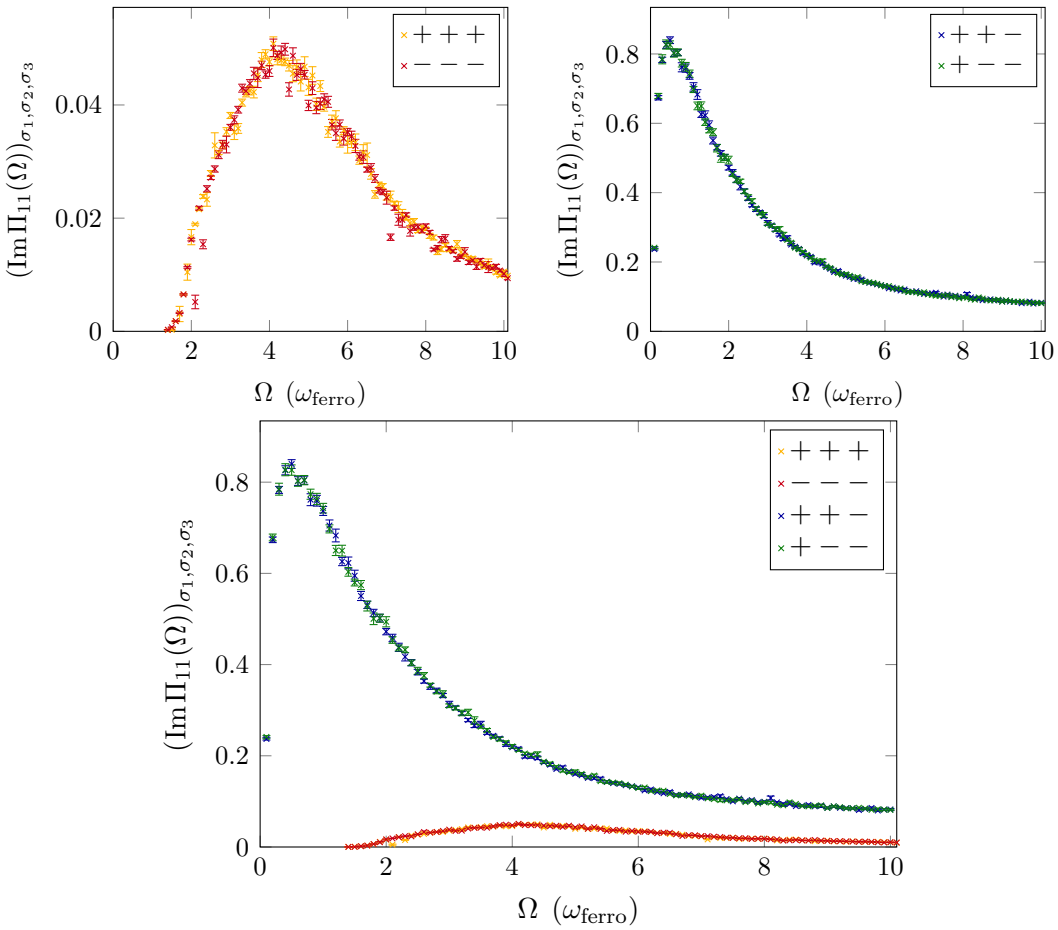

Figure 18: Integration over the separate sum terms

They have a maximum at about $\Omega \simeq 4$.

When we consider the part in $\mathrm{Im}\,\Pi_{\mathrm{diag}}$ that comes from the Bose and the delta functions, one can investigate which triangles contribute to which frequency. For the case $\sigma_1 = \sigma_2 = \sigma_3 = +1$, the smallest frequency possible is for the configuration when all momenta lie in the equatorial plane and build an equilateral triangle, where the sides have length Q_{min}. For the magnetic excitation-field used here the minimal frequency is $\Omega = 1.2$. There is no contribution for lower frequencies from these two terms.

Equilateral triangles in the equatorial plane correspond to skyrmion type fluctuations as discussed previously. For vanishing temperature, i. e. $T = 0$, there are no magnons present. The only process which can then take place is the case with $\sigma_1 = \sigma_2 = \sigma_3 = +1$. The frequency-threshold for $T = 0$ is hence due to exactly the process which was our candidate for the shift in the resonance frequency.

The Bose function part

$$\frac{\epsilon(\vec{q}_1) + \epsilon(\vec{q}_2) + \epsilon(\vec{q}_3)}{\epsilon(\vec{q}_1)\ \epsilon(\vec{q}_2)\ \epsilon(\vec{q}_3)} \tag{6.5}$$

can be maximised by minimising two of the energies by letting them point to

the north pole of the sphere in momentum space with radius Q. However, this configuration contributes to higher frequencies than $\Omega \simeq 4$. Here, triangles with one vector in the equatorial plane and one pointing to the northern hemisphere contribute as well as configurations where one momentum vector vanishes or at least has a significantly small length while the other points towards the northern hemisphere. Nonetheless, the main effect for the maximum is that the phase space grows when increasing the frequency from the minimal frequency. For higher frequencies the number of configurations with low energies, i. e. a big contribution from the Bose function part, shrinks and the value of the integral goes down again.

The discussion of the case $\sigma_1 = \sigma_2 = \sigma_3 = -1$ goes analogously with north and south exchanged.

The upper right plot in figure 18 shows the two cases where one sign differs from the other two. As in the previous case, both cases show the same behaviour. Here, we observe the peak at small frequency ($\Omega \simeq 0.6$). The lower plot in figure 18 shows all four terms in one plot. There it becomes obvious that the cases, where all particles are absorbed or emitted, have a significantly smaller weight than the other two cases. This means that the dominant processes are those where two particles are absorbed and one emitted or two particles are emitted and one absorbed.

Let us, for example, consider the case where $\sigma_1 = \sigma_2 = +1$ and $\sigma_3 = -1$. The part from the Bose functions in $\operatorname{Im}\Pi_{\text{diag}}$ then reads

$$\left| -\frac{\epsilon(\vec{q}_1) + \epsilon(\vec{q}_2) - \epsilon(-\vec{q}_3)}{\epsilon(\vec{q}_1)\,\epsilon(\vec{q}_2)\,\epsilon(-\vec{q}_3)} \right| . \tag{6.6}$$

Again, this can be maximised when $\vec{q}_1$ and $\vec{q}_2$ point to the north pole. Triangles with $\vec{q}_1$ and $\vec{q}_2$ pointing somewhere to the northern hemisphere with angles between them from about 0° to 120° contribute to the peak as well as the cases when one of the vectors $\vec{q}_1$ and $\vec{q}_2$ vanishes, at least almost, and the other points to the north pole. When slightly varying the lengths or angles of the momentum vectors in these configurations, the part stemming from the Bose functions stays large for some time, such that there is a finite phase space volume with high weight around these maximising configurations.

As discussed in section 5, the energy remains flat for quite large angles when surrounding the sphere from the north pole to the south pole (cf. figure 15). It is sufficient that a vector points to the northern hemisphere to approximately minimise $\epsilon(\vec{q})$ and therefore maximise (6.6).

Triangles with $\vec{q}_1$ and $\vec{q}_2$ pointing in nearly the opposite direction, i. e. the angle between them is more than 120°, have almost no contribution. For higher frequencies, here $\Omega \gtrsim 5$, it is not possible to find configurations with two vectors having length Q. Expression (6.6) then decreases rapidly and $\operatorname{Im}\Pi_{\text{diag}}$ becomes small for higher frequencies.

Again, the case of two $\sigma_i = -1$ and one $+1$ follows the same lines, only with north and south exchanged.

6.3. Magnetic field dependence

To compare the susceptibility with the experiments, we need to calculate the self-energy in dependence of the magnetic field. As discussed in subsection 2.2, the magnetic field influences the energy gaps, i. e. $\kappa_\perp$ and $\kappa_\parallel$. The influence of the magnetic field could therefore be described by solving the generalised Brazovskii equations (2.21) and (2.20) for $\kappa_{\parallel/\perp}$. However, solving these coupled self-consistent equations is difficult and leads to numerical problems which could not be solved without bigger efforts. Therefore, we did an ad-hoc fit to the experimental data by Jonas Kindervater to mimic the field dependence of the $\kappa_{\parallel/\perp}$. For 29.1 K we obtained

$$\kappa_\perp(B) = 0.15 + 6.17 \cdot 10^{-12} \left(\frac{B}{\mathrm{mT}}\right)^4 , \tag{6.7}$$

$$\kappa_\parallel(B) = 0.15 + 4.46 \cdot 10^{-11} \left(\frac{B}{\mathrm{mT}}\right)^4 . \tag{6.8}$$

Figure 19 shows the experimental data (dots [20]) and the approximated functions to show that the estimation seems to be reasonable.

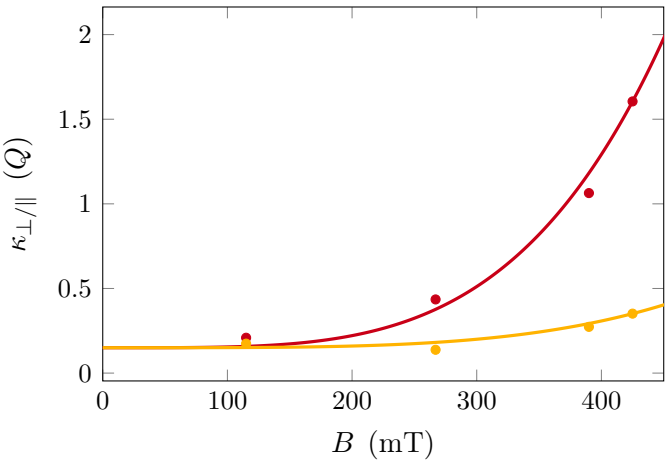

Figure 19: Approximation (line) of the field dependence of the $\kappa_\perp$ (yellow) and $\kappa_\parallel$ (red) at 29.1 K compared to the experimental data (dots) of J. Kindervater [20].

This allows us to calculate the imaginary part of the self-energy for systematically varied magnetic fields. Since the aim is to calculate the maximum frequency as a function of the magnetic field, we increase the field in steps of 10 mT and calculate the self-energy for each of these fields.

The results for $\mathrm{Im}\,\Pi_{11}(\Omega)$ are presented in figure 20. We observe the peak discussed previously for smaller magnetic fields. When reaching a field where $\kappa_\parallel$ becomes larger than 1, no peak can be observed anymore. The imaginary part of the self-energy then stays constant for a long time after an increase at the beginning. The corresponding field is 371.5 mT.

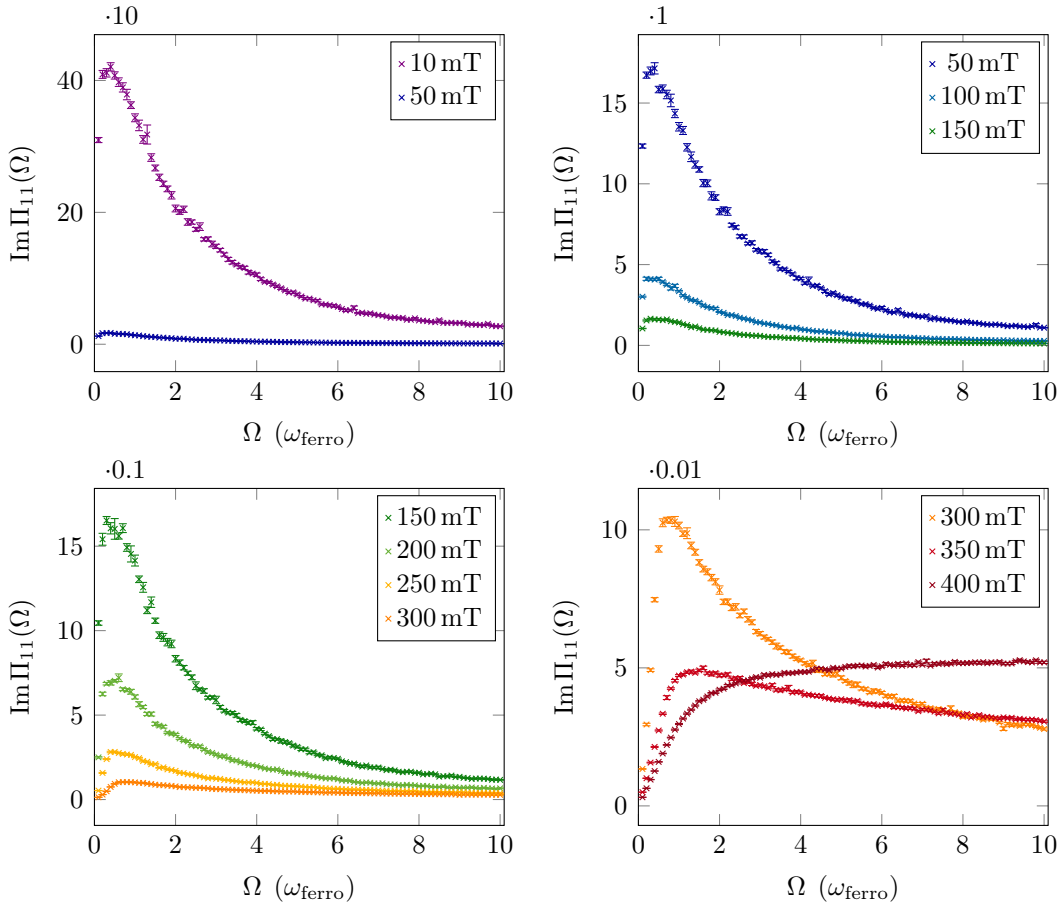

Figure 20: Imaginary part of the self-energy as a function of the frequency for different magnetic fields: violet: 10 mT; blue: 50 mT; turquoise: 100 mT; dark green: 150 mT; light green: 200 mT; yellow: 250 mT; orange: 300 mT; red: 350 mT; dark red: 400 mT.

The integration results for all fields do not approach zero very fast. We will show in the next subsection that they indeed converge to a finite value. They will finally go to zero when reaching the momentum cutoff at high frequencies.

6.4. Asymptotic behaviour for high frequencies

The imaginary parts of the diagonal elements of the self-energy do not converge to zero very fast. They are even close to constant for a long time before decaying due to the momentum cutoff in an energy region of the order $\Omega \sim q_{\mathrm{max}}^2$.

To investigate their behaviour for large frequencies, one has to understand what is happening for large momenta. Therefore, we examine the asymptotic behaviour in this limit, i. e. for $\Omega \to \infty$. When the frequency is large, the energies, and thus the

momenta, have to be large due to the delta function. For the energies we find

$$\epsilon_{\pm}(\vec{q}) = \frac{1}{1+\kappa_\perp^2}\left(-2q_3 \pm \sqrt{\left(1+q^2+\kappa_\perp^2\right)^2 - 4\left(q_1^2+q_2^2\right)\frac{1+q^2+\kappa_\perp^2}{1+q^2+\kappa_\parallel^2}}\right)$$
$$\overset{q^2\gg 1+\kappa_\parallel^2}{\longrightarrow} \pm\frac{q^2}{1+\kappa_\perp^2}\,. \tag{6.9}$$

The matrix element part is approximated by a constant since the nominator as well as the denominator of the matrices $a_\pm(\vec{q})$ with the asymptotic performance of the energies has the maximal power of q^4,

$$\operatorname{Re} A_{\sigma_1,\sigma_2,\sigma_3}(\vec{q}_1,\vec{q}_2,\vec{q}_3) \overset{q^2\gg 1+\kappa_\parallel^2}{\longrightarrow} \frac{\sigma_1\sigma_2\sigma_3}{8\left(1+\kappa_\perp^2\right)^3}\cdot\begin{cases}0 & \sigma_2=\sigma_3\\ 12 & \sigma_1=\sigma_2\neq\sigma_3\\ 4 & \sigma_1=\sigma_3\neq\sigma_2\end{cases}. \tag{6.10}$$

In this limit we can solve the integral (5.20) analytically. For further simplification, we only consider the case $\sigma_1=\sigma_2=+1$ and $\sigma_3=-1$ and, as before, positive frequencies. The integration over the other summands can be performed analogously. The integral we want to solve reads

$$\operatorname{Im}\Pi_{11} \overset{q^2\gg 1+\kappa_\parallel^2}{\longrightarrow} \frac{2\pi}{\beta^2}\sum_{\vec{q}_1,\vec{q}_2,\vec{q}_3} -\frac{\epsilon(\vec{q}_1)+\epsilon(\vec{q}_2)-\epsilon(-\vec{q}_3)}{\epsilon(\vec{q}_1)\,\epsilon(\vec{q}_2)\,\epsilon(-\vec{q}_3)}\operatorname{Re} A_{\sigma_1,\sigma_2,\sigma_3}(\vec{q}_1,\vec{q}_2,\vec{q}_3)$$
$$\cdot\,\delta\big(\omega-\epsilon(\vec{q}_1)-\epsilon(\vec{q}_2)+\epsilon(-\vec{q}_3)\big)\,\delta_{\vec{q}_1+\vec{q}_2+\vec{q}_3,0}\,. \tag{6.11}$$

As in section 5 we have used the symmetries of the energies ϵ_+ and ϵ_-, $\epsilon_-(\vec{q}) = -\epsilon_+(-\vec{q}) \equiv -\epsilon(-\vec{q})$. Exploiting the delta function, this can be rewritten as

$$\operatorname{Im}\Pi_{11} \overset{q^2\gg 1+\kappa_\parallel^2}{\longrightarrow} \frac{2\pi}{\beta^2}\int d^3q_1\,d^3q_2\left[-\frac{\omega\operatorname{Re} A_{\sigma_1,\sigma_2,\sigma_3}(\vec{q}_1,\vec{q}_2,-\vec{q}_1-\vec{q}_2)}{\epsilon(\vec{q}_1)\,\epsilon(\vec{q}_2)\,\epsilon(-\vec{q}_1-\vec{q}_2)}\right.$$
$$\left.\cdot\,\delta\big(\omega-\epsilon(\vec{q}_1)-\epsilon(\vec{q}_2)+\epsilon(\vec{q}_1+\vec{q}_2)\big)\right]. \tag{6.12}$$

Since we only consider the limit of large momenta, we only integrate over $|\vec{q}_i^{\,2}| \gg 1+\kappa_\parallel^2$. We choose our lower integration boundary to be $q_{\min} = N\sqrt{1+\kappa_\perp^2}$ where N is a sufficiently large constant to ensure that the approximations are valid. Using spherical coordinates and the approximations for the energies, and further performing the integrals over all angles except for the relative angle of the two momenta, we obtain

$$\operatorname{Im}\Pi_{11} \overset{q^2\gg 1+\kappa_\parallel^2}{\longrightarrow} \frac{16\pi^3}{\beta^2}\int_0^\pi d\theta\,\sin(\theta)\int_{N\sqrt{1+\kappa_\perp^2}}^\infty dq_1\int_{N\sqrt{1+\kappa_\perp^2}}^\infty dq_2\,\frac{3\,\omega\,\delta\left(\omega\left(1+\frac{2q_1q_2cos(\theta)}{\omega(1+\kappa_\perp^2)}\right)\right)}{2\left(q_1^2+q_2^2+2q_1q_2cos(\theta)\right)}\,. \tag{6.13}$$

We can now rescale the momenta with $q_{1/2} \to \sqrt{\omega(1+\kappa_\perp^2)}\,q_{1/2}$ and get rid of all

frequencies in the integrand.

$$\mathrm{Im}\,\Pi_{11} \overset{q^2 \gg 1+\kappa_\parallel^2}{\longrightarrow} \frac{16\pi^3}{\beta^2(1+\kappa_\perp^2)} \int_0^\pi d\theta \sin(\theta) \int_{N/\sqrt{\omega}}^\infty dq_1 \int_{N/\sqrt{\omega}}^\infty dq_2 \frac{3\,\delta\big(1+2q_1q_2cos(\theta)\big)}{2\left(q_1^2+q_2^2+2q_1q_2cos(\theta)\right)} \tag{6.14}$$

For $\omega \to \infty$ the lower integration boundaries go to 0. Therefore, the result will be independent of ω and N as we observe it to be in the numerical calculations for high frequencies.

$$\mathrm{Im}\,\Pi_{11} \overset{q^2 \gg 1+\kappa_\parallel^2}{\longrightarrow} \frac{16\pi^3}{\beta^2(1+\kappa_\perp^2)} \int_0^\pi d\theta \sin(\theta) \int_0^\infty dq_1 \int_0^\infty dq_2 \frac{3\,\delta\big(1+2q_1q_2cos(\theta)\big)}{2\left(q_1^2+q_2^2+2q_1q_2cos(\theta)\right)} \tag{6.15}$$

The remaining integral can be solved by using the delta function for the integration over the angle and then integrating over the radii. The result is a number, namely

$$\mathrm{Im}\,\Pi_{11} \overset{q^2 \gg 1+\kappa_\parallel^2}{\longrightarrow} \frac{1}{\beta^2} \frac{16\pi^3}{1+\kappa_\perp^2} \cdot 2.78\,. \tag{6.16}$$

We can make a prediction for the constant to which $\mathrm{Im}\,\Pi_{11}(\Omega)$ converges for high frequencies within this approximation by including all other combinations of σ_i. Figure 21 shows examplarily the case for 100 mT.

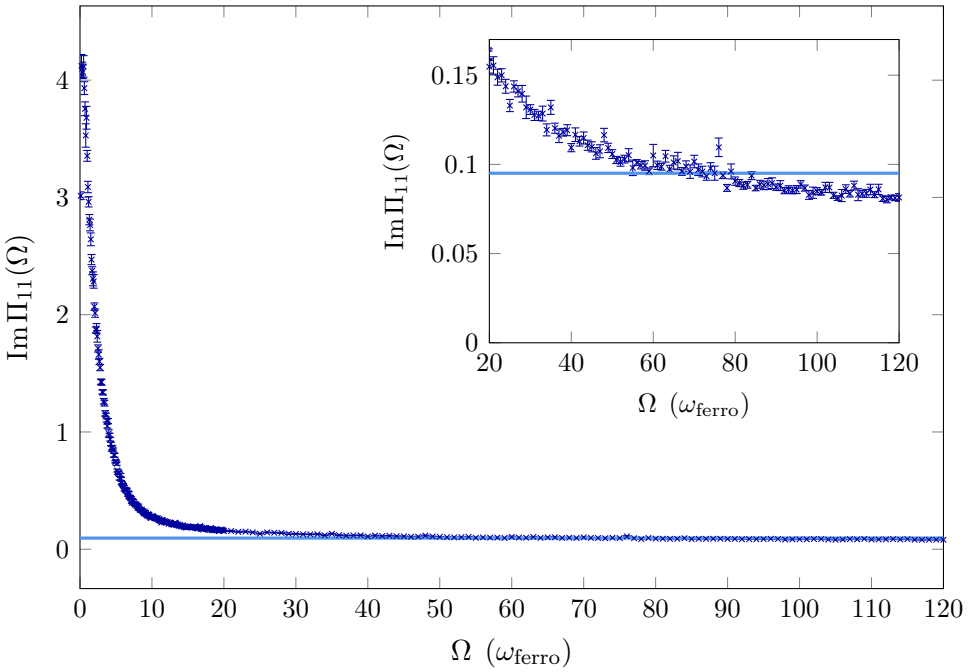

Figure 21: Comparison between the calculation in the limit $q^2 \gg 1+\kappa_\parallel^2$ (light blue line) and $\mathrm{Im}\,\Pi_{11}(\Omega)$ (dark blue crosses) at 100 mT.

We observe that the constant corresponds quite well to the value to which the full

integral converges. However, this prediction only works for sufficiently small fields. For higher magnetic fields there are deviations from the calculated constant up to a factor of five for 400 mT.

Not included in this estimation are triangles with two momenta being large and one small or all momenta being small. It is possible to show, that these configurations do not contribute for $\omega \to \infty$. These cases are sketched in Appendix B.

For high energies, there exists an increasing number of configurations of the momenta that are not considered in the numerical integration due to the cutoff $q_{\max} = 100$. Thus, $\mathrm{Im}\,\Pi_{11}$ falls below the value of this calculation for the asymptotic behaviour at some point at high frequencies. Furthermore, we slightly overestimated the constant since we included also triangles where $\vec{q}_1$ and $\vec{q}_2$ have approximately the same length and show roughly in the same direction. Then, $\vec{q}_3$ is small and the estimation that $q_3 \ll 1 + \kappa_\parallel$ is not valid.

There are different processes which ensure that the integral nevertheless decays for high frequencies. For high energies, the approximation of the Bose functions as an expansion up to second order is not valid anymore. It is necessary to include all orders for high energies since there $\beta\epsilon(\vec{q})$ is not small anymore.

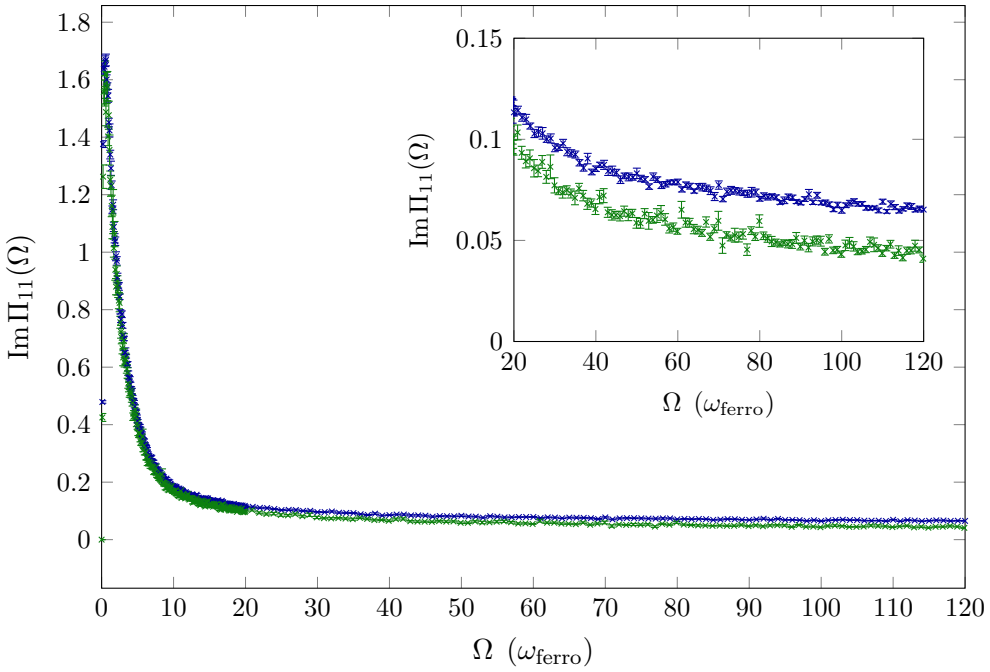

Figure 22: $\mathrm{Im}\,\Pi_{11}(\Omega)$ with the full Bose functions (green) and with series expansion of the Bose functions up to order β^{-2} (blue).

Figure 22 shows the case with the full Bose functions (green) compared to the approximated one (blue). One can see that the effect is quite small. Since the energies are measured in units of $\hbar\omega_{\mathrm{ferro}}$, β has to be dimensionless and reads

$$\beta = \frac{g\mu_B B}{k_B T} \,. \tag{6.17}$$

For $B = 115\,\mathrm{mT}$ and $T = 29.1\,\mathrm{K}$, one gets $\beta = 0.0051$. Within the energy region plotted in figure 22 the approximation of the Bose function by the series expansion up to order β^{-2} stays valid. Higher order terms become more important for frequencies larger than $\Omega \sim 200$.

Furthermore, the high energy cutoff, i. e. the cutoff in the momentum space, also forces the integral to converge to zero for high frequencies. The cutoff could be lowered, for example, by introducing a q^4-term to the Lagrangian which corresponds to a higher order kinetic term.

In a more realistic model the integral should converge to zero instead of a finite constant for high frequencies.

6.5. Real parts and off-diagonal elements of the self-energy

In the next section we can now finally calculate the correction of the susceptibility due to the self-energy and compare the results with the experimental data. The imaginary part of the susceptibility contains the whole self-energy and not only $\mathrm{Im}\,\Pi_{11}$, which was discussed in this section so far. The off-diagonal (1,2)- and (2,1)-element needs to be calculated as well as the real part of the self-energy.

As discussed in the previous section, we can calculate the real part of the diagonal element directly or by using the Kramers-Kronig relation. Both methods show slight deviations from each other due to the different numerical steps. In particular, using Kramers-Kronig produces errors when the original function $\mathrm{Im}\,\Pi$ has not converged to zero, yet.

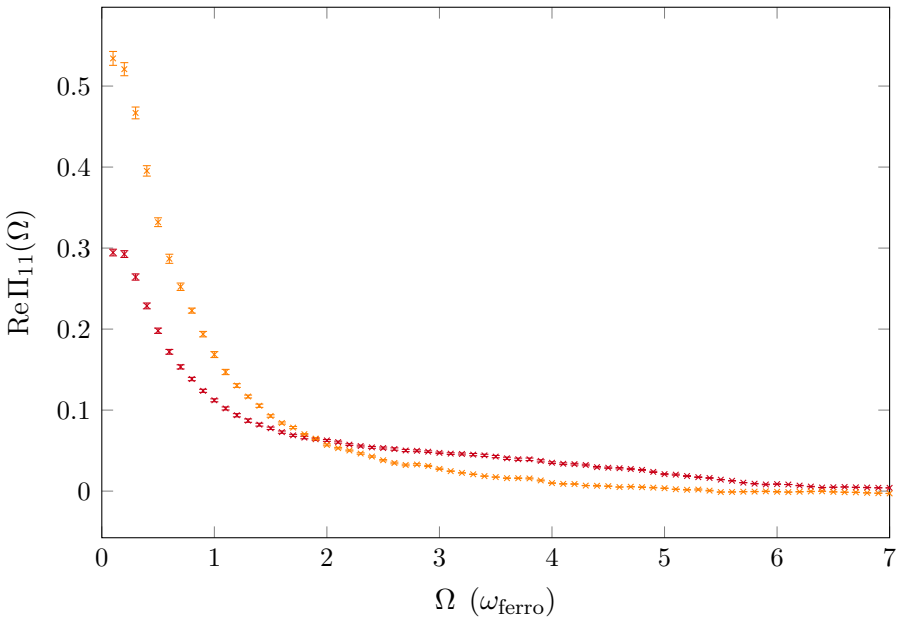

Figure 23: $\mathrm{Re}\,\Pi_{11}(\Omega)$ calculated directly (red) and with the Kramers-Kronig realtion (orange) at 250 mT

Figure 23 shows the real part of the diagonal element calculated with the different methods. The red curve is calculated directly like it is presented in equation (5.27). The orange curve is calculated by using the Kramers-Kronig relation for the imaginary part. We can show that these methods are equivalent. However, both curves do not match exactly. This indicates that the integration intervals do not match due to the different numerical starting points.

We observe a maximum at zero frequency in both cases. One reason for this is discussed in [1]. Equation (B38) in [1] gives an estimate for the correction due to the second order diagram to the Brazovskii equation at zero magnetic field. It is argued that, without the second order diagram, the energy gap Δ at $B = 0$ scales like

$$\Delta = r - JQ^2 + \frac{\varepsilon_{\mathrm{Gi}}^{3/2}}{\sqrt{\Delta}} , \tag{6.18}$$

which corresponds to equation (4.7).The Ginzburg energy $\varepsilon_{\mathrm{Gi}}$ is defined as

$$\varepsilon_{\mathrm{Gi}} = \left(\frac{5}{36\pi} \frac{u\, k_B T\, Q^3}{\sqrt{JQ^2}} \right)^{2/3} . \tag{6.19}$$

The second order diagram gives rise to a correction of the right hand side of (6.18) of the form

$$\delta\Delta \sim \frac{\varepsilon_{\mathrm{Gi}}^3}{\Delta^{3/2}\sqrt{JQ^2}} . \tag{6.20}$$

This holds for $\Omega = 0$. For $\kappa \to 0$ and thus $\Delta \to 0$, there will be a divergence which

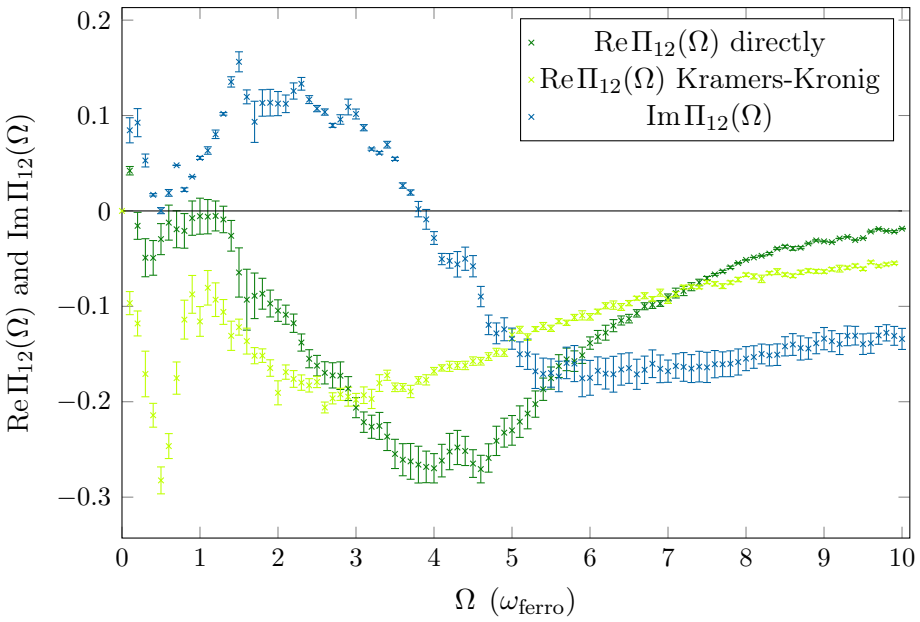

Figure 24: (1,2)-element at 150 mT: $\mathrm{Re}\,\Pi_{12}$ calculated directly (light green), $\mathrm{Re}\,\Pi_{12}$ calculated with Kramers-Kronig (dark green) and $\mathrm{Im}\,\Pi_{12}$ (blue)

leads to a maximum at $\Omega = 0$. This explains the large values of $\mathrm{Re}\,\Pi_{11}(\Omega)$ at small frequencies for small magnetic fields.

However, the maximum of the orange curve is nearly twice as high as the red one. This is due to problems with Kramers-Kronig. The imaginary part of Π_{11} does not converge to zero very fast, as discussed in the previous section. Kramers-Kronig can only be used for functions which converge to zero. The imaginary part converges only for really high frequencies to zero. The frequency calculation was just cut off at some point. The non-zero constant value for high frequencies leads to the much higher maximum with this method. For the calculation of the susceptibility we will use the direct method, which was used for the red curve.

Not all off-diagonal elements vanish. The (1,2)- and (2,1)-element renormalise the ferromagnetic resonance frequency. As for the diagonal elements, we can calulate the real part directly or by the Kramers-Kronig relation from the imaginary part. Like before, the result is not exactly the same. Figure 24 shows the imaginary part of the off-diagonal element (blue) and the real part calculated with Kramers-Kronig (dark green) and directly (light green). We will use the direct method to calculate the susceptibility to avoid the convergence problems of Kramers-Kronig.

7. Calculation of the susceptibility

In this section, we will eventually calculate the imaginary part of the susceptibility and compare the position of its maximum to the experimental measurements.

7.1. Susceptibility for different magnetic fields

The susceptibility can be calculated from the bare Green's function χ_0 and the self-energy Π using the relation

$$\chi^{-1} = \chi_0^{-1} - \Pi \,. \tag{7.1}$$

Up to now, everything was calculated in dimensionless units and the pre-factor of the self-energy coming from perturbation theory was not yet included. Now, however, it is needed, since we want to compare the self-energy to the Green's function χ_0.

To get the original inverse Green's function in the right physical dimensions of energy density, one has to multiply by JQ^2. The experimental values of the parameters are given in [1]. The pitch length is $Q = 0.039\,\text{Å}^{-1}$ and the coupling constant $J = 2.8\,\text{meV/Å}$.

In the self-energy there are three Green's functions multiplied. This gives an overall pre-factor of $(JQ^2)^{-3}$. The combinatorial factor of the second order diagram in this case is $4 \cdot 4 \cdot 2$. From the expansion up to second order we get $1/(\beta^2 V^2)(u/4!)^2$ with $\beta = (k_B T)^{-1}$. To reduce confusion, we write the former β from the expansion of the Bose functions explicitly as $(\hbar\omega_{\text{ferro}})/(k_B T)$. From going to the continuum limit, and from performing the integration over dimensionless momenta there is a further factor of $(Q^3 V/(2\pi)^3)^2$ present. The imaginary part of the diagonal terms of self-energy, for example, then reads

$$\begin{aligned}
\operatorname{Im}\Pi_{\text{diag}}(0,\Omega) = &- \left(\frac{u}{4!}\right)^2 4 \cdot 4 \cdot 2 \cdot \pi \, (JQ^2)^{-3} \frac{1}{\beta^2} \left(\frac{Q^3}{(2\pi)^3}\right)^2 \left(\frac{\hbar\omega_{\text{ferro}}}{k_B T}\right)^{-2} \\
&\cdot \sum_{\vec{q}_1,\vec{q}_2,\vec{q}_3} \sum_{\sigma_1,\sigma_2,\sigma_3=\pm} \frac{\sigma_1\epsilon(\sigma_1\vec{q}_1) + \sigma_2\epsilon(\sigma_1\vec{q}_2) + \sigma_3\epsilon(\sigma_1\vec{q}_3)}{\sigma_1\epsilon(\sigma_1\vec{q}_1)\;\sigma_2\epsilon(\sigma_2\vec{q}_2)\;\sigma_3\epsilon(\sigma_3\vec{q}_3)}\, \delta_{\vec{q}_1+\vec{q}_2+\vec{q}_3,0} \\
&\cdot \operatorname{Re} A_{\sigma_1,\sigma_2,\sigma_3}(\vec{q}_1,\vec{q}_2,\vec{q}_3) \Big[\delta\big(\Omega - \sigma_1\epsilon(\sigma_1\vec{q}_1) - \sigma_2\epsilon(\sigma_2\vec{q}_2) - \sigma_3\epsilon(\sigma_3\vec{q}_3)\big) \\
&- \delta\big(\Omega + \sigma_1\epsilon(\sigma_1\vec{q}_1) + \sigma_2\epsilon(\sigma_2\vec{q}_2) + \sigma_3\epsilon(\sigma_3\vec{q}_3)\big)\Big] \,.
\end{aligned} \tag{7.2}$$

In [1] there is given a value for u, namely $u = 0.32\,\text{meV/Å}^3$. However, we are applying perturbation theory in u, so it needs to be small compared to $JQ^2 \simeq 0.004\,\text{meV/Å}^3$. Otherwise, the approximation is not valid. Thus we have to use a much smaller value u to calculate χ.

The inverse Green's function with momentum $\vec{q} = 0$ defines χ_0^{-1}. We analytically

continue $i\Omega \to \Omega + i\varepsilon$.

$$\chi_0^{-1}(0,\Omega) = JQ^2 \begin{pmatrix} 1+\kappa_\perp^2 & -i(1+\kappa_\perp^2)(\Omega+i\varepsilon) & 0 \\ i(1+\kappa_\perp^2)(\Omega+i\varepsilon) & 1+\kappa_\perp^2 & 0 \\ 0 & 0 & 1+\kappa_\parallel^2 \end{pmatrix} \tag{7.3}$$

The self-energy has only off-diagonal entries for the (1,2)- and the (2,1)-element and therefore, the (3,3)-component of the susceptibility decouples from the rest. The (2,2)-element and the (1,1)-element are equal. It is sufficient to calculate the (1,1)-element, which reads

$$\begin{aligned} \operatorname{Im}\chi_{11}(\Omega) =& \operatorname{Im}\Bigg[\Big(JQ^2\big(1+\kappa_\perp^2\big) - \big(\operatorname{Re}\Pi_{11}(\Omega) + i\operatorname{Im}\Pi_{11}(\Omega)\big)\Big) \\ & \cdot \Big(\big(JQ^2(1+\kappa_\perp^2) - (\operatorname{Re}\Pi_{11}(\Omega) + i\operatorname{Im}\Pi_{11}(\Omega))\big)^2 \\ & + \big(i(1+\kappa_\perp^2)(\Omega+i\varepsilon) + (\operatorname{Re}\Pi_{12}(\Omega) + i\operatorname{Im}\Pi_{12}(\Omega))\big)^2\Big)^{-1}\Bigg], \end{aligned} \tag{7.4}$$

where $\varepsilon \ll 1$ assures convergence.

For a small perturbation parameters $u = 0.0032\,\mathrm{meV/Å^3}$ and high enough fields, we find a sharp peak at the ferromagnetic resonance frequency $\Omega = 1$. This peak is slightly broadened due to the self-energy. For smaller fields, the weight of the electron-spin resonance shrinks since it is proportional to the magnetic field (cf. equation (3.30)). The self-energy can then gain influence, which leads to the peak position being shifted. As will be discussed later, the maximum first approaches zero before it is shifted to higher frequencies $\Omega > 1$. Figure 25 examplarily shows the broadened delta peak at a higher field and the shifted maximum position for smaller fields for this small value of u.

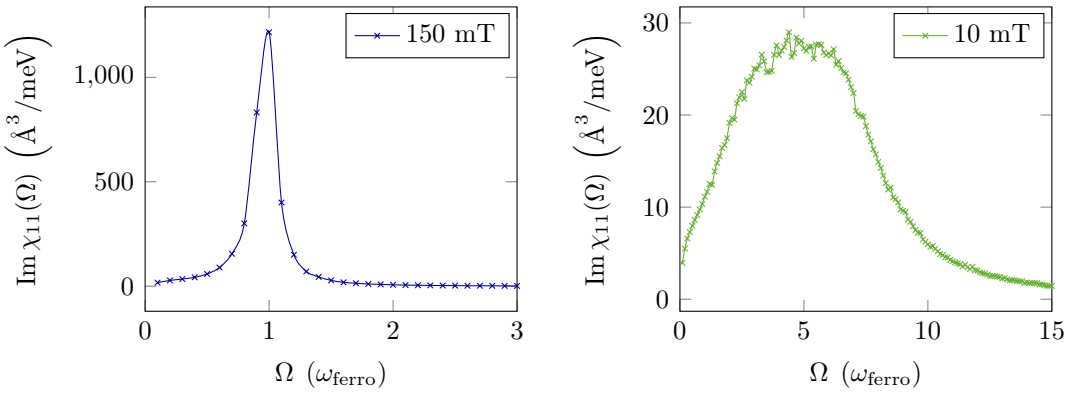

Figure 25: Susceptibility with $u = 0.0032\,\mathrm{meV/Å^3}$ at two magnetic fields. At higher fields (left, here at 150 mT), the delta peak at ω_{ferro} is broadened by Π but does not change the position. At small fields (right plot at 10 mT), the peak position is shifted to higher frequencies.

Figure 26 shows the susceptibility as a function of frequency for different magnetic

fields for two different larger perturbation parameters u. The first two plots are for $u \simeq 0.0081\,\mathrm{meV/\AA^3}$, and the lower row is for $u \simeq 0.015\,\mathrm{meV/\AA^3}$. The experimental value given in [1] is $u \simeq 0.32\,\mathrm{meV/\AA^3}$. To get to a regime where perturbation theory becomes valid, u has to decrease at least by a factor of 20 compared to the experimental value. Even the values for u used here are quite big compared with the value of JQ^2.

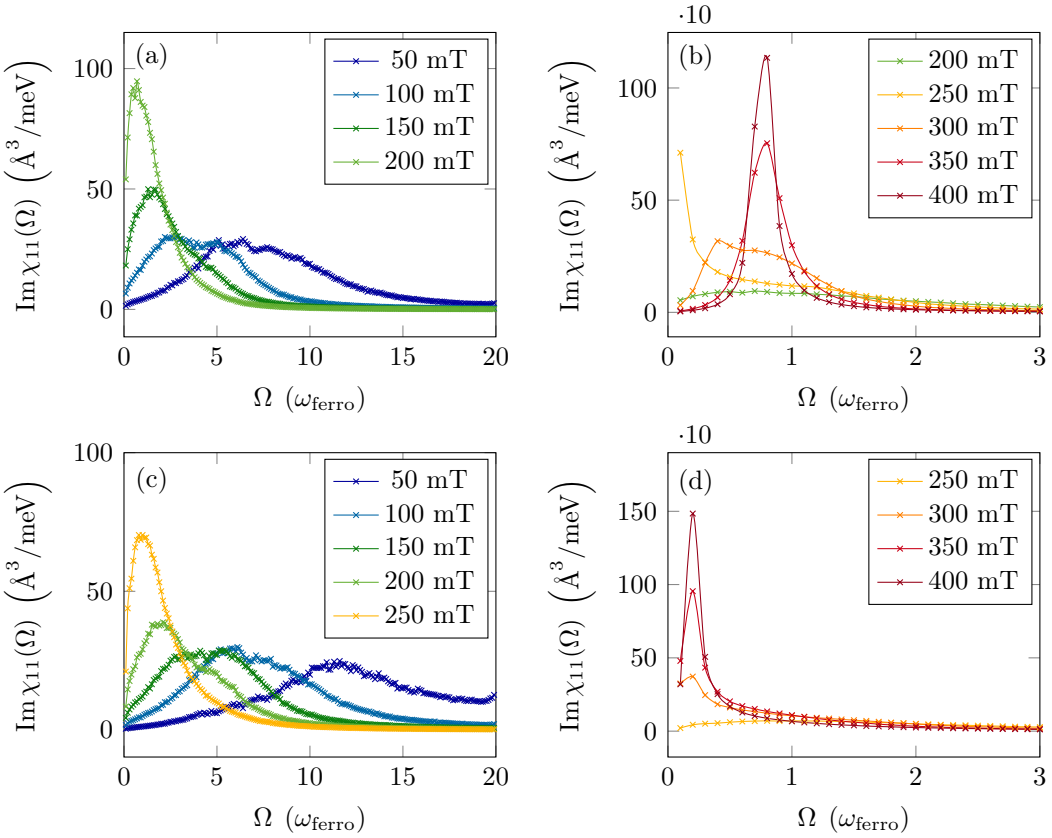

Figure 26: Susceptibility for different magnetic fields and different perturbation parameters u:
(a) & (b): $u \simeq 0.0081\,\mathrm{meV/\AA^3}$,
(c) & (d): $u \simeq 0.015\,\mathrm{meV/\AA^3}$.

In both cases for low fields the maximum is at high frequencies. When increasing the field, the maximum position approaches the ferromagnetic resonance frequency, which is at $\Omega = 1$ here.

When continuing to increase the field, the maximum position drops below 1. The second plot for each u shows the behaviour for larger fields. We observe that the maximum even approaches zero. This is unrealistic since the electron-spin resonance frequency is a reference point for the peak position. This strange behaviour mainly comes from the huge value of $\mathrm{Re}\,\Pi_{11}$ for $\Omega = 0$. The constant parts contribute to the integrals and increase the value for small Ω. However, the calculation should not predict unphysical behaviour. This issue requires further investigation.

For higher magnetic fields the maximum position shifts towards $\Omega = 1$ again. This is what we expect, because for high fields we enter the paramagnetic phase. The Dzyaloshinskii-Moriya interaction then looses importance and the resonance frequency becomes exactly ω_{ferro}. The self-energy leads to a broadening of the peak but not to a shift.

At which fields the maximum position reaches the ferromagnetic resonance frequency, decreases to zero and approaches $\Omega = 1$ again depends on the value of the perturbation parameter u. Since we do not have any experimental input for this, we cannot make any quantitative statements that could be compared to the experiments.

7.2. Discussion of the maximum frequency

To answer the question whether the fluctuations addressed by the second order self-energy diagram give rise to the shift of the resonance frequency in the FD regime, one has to determine the maximum position of the imaginary part of the susceptibility.

To achieve that, we fit a Gaussian to the susceptibility for each magnetic field. The fit function is of the form

$$f(x) = n \cdot \exp\left[-a(x-b)^2\right] + c\,. \tag{7.5}$$

There are four fit parameters: the normalisation n, the factor a in the exponent, which relates to the variance σ via $\sigma = 1/\sqrt{2a}$, the peak position b, and the background c.

In the regime where the maximum position approaches zero, it is not possible to make a reasonable fit to the susceptibility. It becomes possible though for higher fields. However, due to the small variance of the peak there, the fitting results are not totally convincing. The values for the peak positions are good but the results for the variances should not be taken too serious in this regime for the two larger values of u.

The fitting results for the maximum position, which corresponds to the fit parameter b, are represented by the red dots in figure 27. For high magnetic fields the influence of the fluctuations is weak and the weight of the electron-spin resonance is big. The correction of the susceptibility due to the second order diagram of the self-energy is therefore small. This is the paramagnetic regime. When coming from high magnetic fields we observe that the peak position is close to the ferromagnetic resonance frequency for sufficiently small u. For $u \simeq 0.0032\,\text{meV}/\text{Å}^3$ it even lies exactly at the ferromagnetic resonance frequency. The peaks are only broadened by the self-energy in this case.

When decreasing the magnetic field, we run into troubles described in the previous section. The maximum position goes to zero, and there is no reasonable fit possible. This is due to the large contribution of $\operatorname{Re}\Pi_{11}(0)$.

When further decreasing the magnetic field, the maximum position starts to shift to higher frequencies. For $u \simeq 0.015\,\mathrm{meV/Å^3}$ this is at about 270 mT, for $u \simeq 0.081\,\mathrm{meV/Å^3}$ at around 190 mT and for $u \simeq 0.0032\,\mathrm{meV/Å^3}$ at approximately 20 mT. The resonance frequency even increases for a decreasing magnetic field up to a maximum. Then, it decreases slightly. However, the frequencies are still much higher than the ferromagnetic resonance frequency at these magnetic fields.

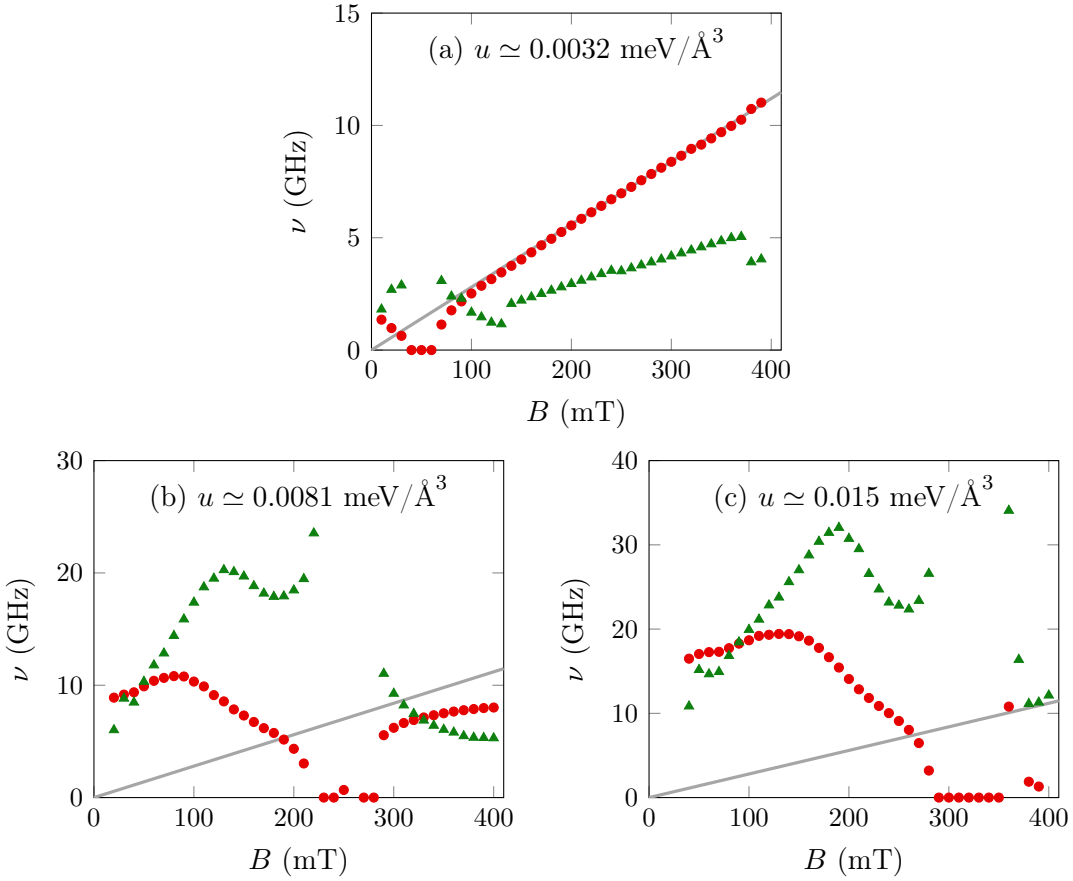

Figure 27: Peak position and FWHM of the susceptibility for different u. The gray line denotes $\omega_{\mathrm{ferro}}(B)$, the red points mark the peak positions and the green triangles the full width at half maximum.

Figure 28 shows the corresponding experimental results at $T = 29\,\mathrm{K}$. $\kappa_\perp$ and $\kappa_\parallel$ we used in the calculation were measured at $T = 29.1\,\mathrm{K}$. The gray line also denotes the ferromagnetic resonance frequency in the field polarised region and corresponds to the gray line in figure 27. The crossover to the FD regime in this case takes place at about 400 mT. We cannot modify the perturbation parameter u such that the beginning of the shift to higher frequencies in the calculation is also at 400 mT without leaving the region where the perturbation theory is valid. In the experiments the maximum position approximately stays constant for a range of the magnetic field range between 150 and 400 mT. This does not correspond to the results of the calculation. Here, the frequency is shifted to much higher values than in the experiment. The increase of the frequency for small fields in the experiments

can be explained by the entering of the helical phase.

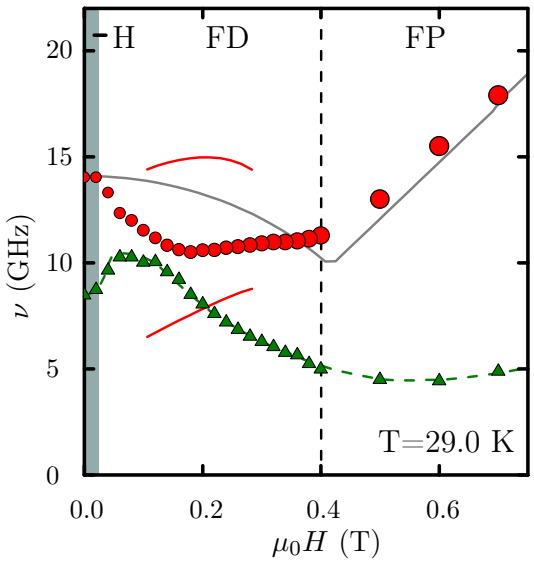

Figure 28: Resonance frequency as a function of magnetic field measured by I. Stasinopoulos [4]

The green triangles in figure 28 correspond to the full width at half maximum of the peak. We can compare these widths to the ones of the fitted bumps shown by the green triangles in figure 27. In the experiments the width is always smaller than the peak position. In the field polarised phase it is approximately constant and starts to increase when entering the FD regime. We find this for the case of $u \simeq 0.0032\,\mathrm{meV/\AA^3}$, too. As described above, it was not possible to make reasonable fits for the paramagnetic regime for larger u. Therefore, the widths in figures 27b and c are jumping around a lot in this region.

When entering the FD regime the peak broadens in the experimental results in figure 28 as well as in the theoretical ones in figure 27. For $u \simeq 0.015\,\mathrm{meV/\AA^3}$ at about 250 mT, for $u \simeq 0.0081\,\mathrm{meV/\AA^3}$ at about 200 mT and for $u \simeq 0.0032\,\mathrm{meV/\AA^3}$ at about 20 mT, we observe an increase of the widths in all cases. It reaches a maximal width and then decreases again. However, these widths are huge compared to the ferromagnetic resonance (gray line) and also to the maximum positions. This is in contrast to the experiments. On the one hand, this is due to the problems with the fitting of the calculated susceptibilities. On the other hand, it means that we can barely call these fitted broad features peaks at all.

Part IV. Conclusion

Chiral paramagnets have been well studied over the past years. One special phase only arising in chiral magnets is the so called fluctuation disordered regime. In this phase space region three-magnon processes give rise to a shift of the resonance frequency compared to in the paramagnetic phase.

The aim of this thesis was to investigate the influence of strong fluctuations in the fluctuation disordered regime. We examined the impact on the imaginary part of the susceptibility and, therefore, on the resonance frequency measured in experiments. These correlations are caused by the Dzyaloshinskii-Moriya interaction present in chiral magnets. We calculated the self-energy using perturbation theory up to second order in the parameter u, which is the pre-factor of the ϕ^4-term in the Ginzburg-Landau theory. We calculated the correction of the imaginary part of the susceptibility induced by the self-energy.

Without the correction to the second order self-energy diagram, the peak position remains at the electron-spin resonance frequency

$$\omega_{\text{ferro}} = \frac{g\mu_B B}{\hbar} \ .$$

Here, only one magnon is involved. The second order diagram includes three magnon processes. For finite temperature, processes where two magnons are absorbed and one is emitted or where two magnons are emitted and one is absorbed dominate the self-energy. Processes with three quasi-particles being absorbed or emitted contribute only insignificantly.

At small magnetic fields we observe that the position of the maximum of the imaginary part of the susceptibility is shifted to higher frequencies compared to the electron-spin resonance frequency. For higher magnetic fields when entering the paramagnetic regime, the peak position approaches the ferromagnetic resonance. The Dzyaloshinskii-Moriya interaction becomes negligible and the chiral magnet behaves like an ordinary paramagnet. However, in the calculation presented in this thesis the paramagnetic behaviour is not reproduced exactly. We run into troubles when increasing the magnetic field. The maximum position approaches zero before being shifted to ω_{ferro} again. This unphysical behaviour can be explained by the large contribution of $\mathrm{Re}\,\Pi_{11}(0)$. It remains an open problem which requires further examination.

The experimental resonance measurements show an approximately constant maximum frequency in the fluctuation disordered regime [4]. This frequency is higher than ω_{ferro}. The shift of the resonance frequency to higher values can be explained by three magnon processes. However, we are not able to reproduce the exact behaviour seen in the experiments. Furthermore, we can only make qualitative

statements since we have to choose a comparably small value for the perturbation parameter u for the final calculation. The experimental value presented in [1] exceeds the ones consistent with perturbation theory.

The original hypothesis was that skyrmion type fluctuations are the reason for the behaviour in the resonance experiments. We proved that this is not the case. The contribution from skyrmionic fluctuations is negligibly small. When increasing the frequency these fluctuations are the first which can arise at zero temperature. However, for higher frequencies they are again not dominant.

Apart from the peak falling below ω_{ferro}, there are more open questions in the calculation, which we were not able to answer yet. The Kramers-Kronig calculation does not precisely agree with the direct calculation of the respective elements. Total agreement and a lower value at zero frequency of $\operatorname{Re}\Pi_{11}$ could also not be achieved by introducing a higher order kinetic term proportional to q^4, which effectively corresponds to an earlier high energy cutoff. Further investigations will be required to solve the problem of the maximum position of $\operatorname{Im}\chi_{11}$ approaching zero.

The Gaussian fits to the susceptibility do not have a high accuracy, especially for magnetic fields between 200 and 400 mT and higher values of u. This leads to mistakes in the maximum positions as well as in the widths. The low accuracy of the fit notwithstanding, the widths obtained from the perturbative calculations are already much bigger than experimentally observed. They are even bigger than the maximum positions.

Obviously, this calculation does not give a full answer to the question what exactly is happening in the fluctuation disordered regime. Higher orders of magnon interaction will contribute. The whole calculation was done at zero momentum, i. e. for a perfectly homogeneous magnetic field. In Munich experiments were performed at finite momentum. In a next step, one could include $\vec{q} \neq 0$ and repeat the calculation. The second diagram in equation (5.12) could no longer be neglected in this case.

We could not reproduce exactly the experimentally observed behaviour. For a totally satisfying explanation of the experiments it is necessary to find a solution such that the maximum position does not approach zero. Nonetheless, we can conclude that in the fluctuation disordered regime three magnon processes give rise to a shift of the resonance frequency to higher frequencies at low magnetic fields.

Part V.
Appendices

A. Derivation of the self-energy in the paramagnet

In this appendix we will outline the derivation of the self-energy for the paramagnet. This is used in the calculation of the electron-spin resonance frequency in subsection 3.1. The calculation is taken from [18].

We consider the effective theory for metals where we have a spin-spin interaction between the electrons. The effective Lagrange density in imaginary time representation is given by

$$\mathcal{L}[\psi,\psi^\dagger] = \psi^\dagger\big(\partial_\tau + \epsilon\big)\psi + \tilde{J}\left(\psi^\dagger\frac{\vec{\sigma}}{2}\psi\right)^2. \tag{A.1}$$

We do a Hubbard-Stratonovich transformation and arrive at

$$\mathcal{L}[\psi^\dagger,\psi,\vec{\varphi}] = \psi^\dagger\big(\partial_\tau + \epsilon\big)\psi + \left(\psi^\dagger\frac{\vec{\sigma}}{2}\psi\right)\cdot\vec{\varphi} - \frac{1}{4\tilde{J}}\,\vec{\varphi}^{\,2}. \tag{A.2}$$

By varying the action with respect to the Hubbard-Stratonovich field, we find

$$\vec{\varphi} = \tilde{J}\,\psi^\dagger\vec{\sigma}\psi\,. \tag{A.3}$$

$\vec{\varphi}$ is the order parameter of the theory. When integrating out the fermionic fields, we get the effective Lagrange density for the order parameter:

$$\mathcal{L}[\varphi] = \frac{1}{2}\,\vec{\varphi}^{\,T}\,G^{-1}\,\vec{\varphi} + \frac{u}{4!}\,\left(\vec{\varphi}^{\,2}\right)^2. \tag{A.4}$$

The inverse Green's function has the form

$$G^{-1} = -\frac{1}{2\tilde{J}} + \Pi\,. \tag{A.5}$$

Therefore, we have to calculate the self-energy Π. Perturbation theory and Fourier transformation lead to

$$\Pi^{ij}(\vec{q},\Omega_n) = \frac{1}{\beta}\sum_{\vec{k}}\sum_{\omega_n}\,\mathrm{Tr}\left[g(\vec{k},\omega_n)\,\sigma^j\,g(\vec{k}+\vec{q},\omega_n+\Omega_n)\,\sigma^i\right], \tag{A.6}$$

where the frequencies ω_n and Ω_n are Matsubara frequencies, σ^i is the i-th Pauli matrix and the electron Green's function is given by

$$g^{-1}_{\alpha\beta}(\vec{k},\omega_n) = i\,\omega_n - \epsilon_k - \vec{\varphi}_0\cdot\vec{\sigma}_{\alpha\beta}\,. \tag{A.7}$$

This holds only in the presence of a finite $\vec{\varphi}_0$, the order parameter at zero frequency. To calculate the self-energy, we need to invert this object:

$$g_{\alpha\beta}(\vec{k},\omega_n) = \sum_{s=\pm 1} \frac{1}{2} \frac{1 - s\,\vec{\varphi}_0 \cdot \vec{\sigma}_{\alpha\beta}}{i\,\omega_n - \epsilon_k + s\,\varphi_0} \,. \tag{A.8}$$

Inserting this into the self-energy, evaluating the trace, and integrating out the Matsubara frequency ω_n leads to

$$\Pi^{ij}(\vec{q},\Omega_n) = \sum_k \sum_{s,s'=\pm 1} \frac{n(\epsilon_k - s\varphi_0) - n(\epsilon_{k+q} - s'\varphi_0)}{i\Omega_n - \epsilon_{k+q} + \epsilon_k + (s+s')\varphi_0} \left[\frac{1+ss'}{2}\delta^{ij} + \frac{s'-s}{2} i\varepsilon^{nji}\phi_0^n \right.$$
$$\left. + ss' \left(\hat{\varphi}_0^j \hat{\varphi}_0^i - \delta^{ij} \right) \right] . \tag{A.9}$$

When φ_0 and q are small, we can approximate $\sum\limits_k -n'(\epsilon_k) \approx \nu$ and arrive at

$$\Pi^{ij}(\vec{q},\Omega_n) = \sum_{\hat{k}} \left[\nu \sum_{s=\pm 1} \frac{\vec{v}\cdot\vec{q} - 2\,s\,\varphi_0}{i\,\Omega_n - \vec{v}\cdot\vec{q} + 2\,s\,\varphi_0} \Big(s\,i\,\varepsilon_{ijn}\,\hat{\varphi}_0^n - \left(\hat{\varphi}_0^i \hat{\varphi}_0^j - \delta^{ij} \right) \Big) \right.$$
$$\left. + \nu \frac{\vec{v}\cdot\vec{q}}{i\Omega_n - \vec{v}\cdot\vec{q}} \hat{\varphi}_0^i\,\hat{\varphi}_0^j \right] . \tag{A.10}$$

ν is the density of states. The velocity $\vec{v}$ has the same direction as $\vec{k}$, i. e. $\vec{v} = v\hat{k}$, where $\hat{k} = \vec{k}/|\vec{k}|$. We choose the magnetic field, and therefore $\vec{\varphi}_0$, to point in the z-direction as we have done in this whole thesis. Then we can write down the self-energy in matrix form.

$$\Pi(\vec{q},\Omega_n) = -\frac{\nu}{2} \begin{pmatrix} 1 & 0 & 0 \\ 0 & 1 & 0 \\ 0 & 0 & 1 \end{pmatrix} + \frac{\nu\,\pi}{4} \frac{|\Omega_n|}{|\vec{q}|} \begin{pmatrix} 0 & 0 & 0 \\ 0 & 0 & 0 \\ 0 & 0 & 1 \end{pmatrix} + i\,\nu \frac{i\,\Omega_n}{2\varphi_0} \begin{pmatrix} 0 & -1 & 0 \\ 1 & 0 & 0 \\ 0 & 0 & 0 \end{pmatrix} . \tag{A.11}$$

This is the form of the self-energy, which is used in subsection 3.1 to calculate the electron-spin resonance frequency.

B. Behaviour for high frequencies - neglected configurations

In subsection 6.4 we investigated the asymptotic behaviour of $\operatorname{Im}\Pi_{11}(\omega)$ in the limit of $\omega \to \infty$. We assumed that $\vec{q}_i \gg 1 + \kappa_\parallel^2$ for all i, i. e. we considered triangles with all three sides being large.

However, triangles which have at least one short side could also contribute. In this appendix we will show that this is not the case.

When all momenta are small, i. e. $\vec{q}_i \lesssim 1 + \kappa_\parallel^2 \ \forall\ i$, there will be no solution for arbitrary large frequencies of the delta function $\delta\big(\omega - \sigma_1\epsilon(\omega - \sigma_1\vec{q}_1) - \sigma_2\epsilon(\sigma_2\vec{q}_2) - \sigma_3\epsilon(\sigma_3\vec{q}_3)\big)$. This means that there is no contribution from small triangles to large energies $\omega \to \infty$.

It is not possible to construct a really large vector by adding two small ones. It remains the case of two large vectors in a configuration such that the third one is small to consider.

For simplicity we assume that $\vec{q}_2$ is the short one, i. e. $|\vec{q}_2| \lesssim 1 + \kappa_\parallel^2$. For $\vec{q}_1$ and $\vec{q}_3$ thus holds the asymptotic behaviour derived in subsection 6.4. The matrix element only depends on $\vec{q}_2$, since the argument of $a_\pm$ still converges to a constant value for $\vec{q}_1$ and $\vec{q}_3$. We will write $\operatorname{Re} A(\vec{q}_2)$ as a short hand notation. Again, we consider the case $\sigma_1 = \sigma_2 = +1$ and $\sigma_3 = -1$. The argument works for any other combination of the σ_i analogously.

We consider the imaginary part of the diagonal element of the self-energy in this limit.

$$\begin{aligned}\operatorname{Im}\Pi_{11} = \frac{2\pi}{\beta^2} \sum_{\vec{q}_1,\vec{q}_2,\vec{q}_3} -\Bigg[&\frac{\epsilon(\vec{q}_1) + \epsilon(\vec{q}_2) - \epsilon(-\vec{q}_3)}{\epsilon(\vec{q}_1)\,\epsilon(\vec{q}_2)\,\epsilon(-\vec{q}_3)} \operatorname{Re} A_{\sigma_1,\sigma_2,\sigma_3}(\vec{q}_1,\vec{q}_2,\vec{q}_3)\,\delta_{\vec{q}_1+\vec{q}_2+\vec{q}_3,0} \\ &\cdot \delta\big(\omega - \epsilon(\vec{q}_1) - \epsilon(\vec{q}_2) + \epsilon(-\vec{q}_3)\big)\Bigg] \\ \longrightarrow \frac{2\pi}{\beta^2} \int d^3q_1 \int d^3q_2 \, &\frac{-\omega \operatorname{Re} A(\vec{q}_2)}{q_1^2\ (\vec{q}_1 + \vec{q}_2)^2\,\epsilon(\vec{q}_2)} \delta\left(\omega - q_1^2 - \epsilon(\vec{q}_2) + (\vec{q}_1 + \vec{q}_2)^2\right).\end{aligned} \tag{B.1}$$

For $\omega \to \infty$, $\epsilon(\vec{q}_2)$ is negligible in the delta function. We introduce spherical coordinates for $\vec{q}_1$, integrate over the angle ϕ and choose θ to be the relative angle between $\vec{q}_1$ and $\vec{q}_2$. This leads to

$$\operatorname{Im}\Pi_{11} \to -\frac{(2\pi)^2}{\beta^2} \int d^3q_2 \, \frac{\operatorname{Re} A(\vec{q}_2)}{\epsilon(\vec{q}_2)} \int_{N\sqrt{1+\kappa_\parallel^2}}^{\infty} dq_1 \int_0^\pi d\theta \sin(\theta) \, \frac{\delta\big(1 + 2q_1q_2\cos(\theta)\big)}{q_1^2 + q_2^2 + 2q_1q_2\cos(\theta)} \ . \tag{B.2}$$

Using the delta function and $q_1 \gg q_2$ allows us to write

$$\operatorname{Im}\Pi_{11} \to -\frac{(2\pi)^2}{2\beta^2}\int d^3q_2\,\frac{\operatorname{Re}A(\vec{q}_2)}{q_2\epsilon(\vec{q}_2)}\int\limits_{N\sqrt{1+\kappa_\parallel^2}}^{\infty} dq_1\int\limits_0^{\pi} d\theta\,\sin(\theta)\frac{\omega\,\delta\Big(\cos(\theta)+\frac{\omega}{2q_1q_2}\Big)}{q_1\,(q_1^2-\omega)}\ . \tag{B.3}$$

Performing the integral over θ gives a lower limit for q_1, which is larger than the original one for sufficiently high frequencies. We can perform the integration over q_1 and obtain

$$\begin{aligned}\operatorname{Im}\Pi_{11} &\to -\frac{(2\pi)^2}{2\beta^2}\int d^3q_2\,\frac{\operatorname{Re}A(\vec{q}_2)}{q_2\epsilon(\vec{q}_2)}\int\limits_{\omega/(2q_2)}^{\infty} dq_1\,\frac{\omega}{q_1\,(q_1^2-\omega)}\\ &= \frac{(2\pi)^2}{4\beta^2}\int d^3q_2\,\frac{\operatorname{Re}A(\vec{q}_2)}{q_2\epsilon(\vec{q}_2)}\left[\ln\left(\frac{\omega^2}{4\,q_2^2}-\omega\right)-\ln\left(\frac{\omega^2}{4\,q_2^2}\right)\right]\\ &\overset{\omega\to\infty}{\longrightarrow} 0\end{aligned} \tag{B.4}$$

In the limit $\omega \to \infty$ we can neglect ω compared to ω^2 and the two logarithmic terms cancel. Therefore, it was reasonable to consider only triangles with solely large momenta in subsection 6.4.

C. Monte Carlo integration

Since it is not possible to analytically integrate the five dimensional integral, at which we arrive in part III, we do it numerically. We use Monte Carlo integration which we implement in a C++ program.

To solve an integral numerically with Monte Carlo integration, one picks N points out of the volume randomly and approximates the integral by a sum over the function values at these points [24].

In the one dimensional case this approximation reads

$$I = \int_0^L dx\, f(x) = \frac{L}{N} \sum_{i=1}^{N} f(x_i) \ , \tag{C.1}$$

with $x_i \in [0, L]$ randomly distributed. The error can be estimated by the standard deviation:

$$\Delta I = \frac{L}{N} \sqrt{\left(\sum_{i=1}^{N} f^2(x_i) \right) - \left(\sum_{i=1}^{N} f(x_i) \right)^2} \ . \tag{C.2}$$

The more points one chooses, i. e. the larger N gets, the better the approximation since the error is proportional to $1/N$.

This method can be directly generalised to higher dimensional integrals. The dimensionality is denoted by n. Now, the points $\vec{x}_i$ are randomly picked out of the volume V, $\vec{x}_i \in V$, and the approximation looks exactly the same as in the one dimensional case:

$$I = \int_V d^n x\, f(\vec{x}) = \frac{V}{N} \sum_{i=1}^{N} f(\vec{x}_i) \ . \tag{C.3}$$

The error is estimated by

$$\Delta I = \frac{V}{N} \sqrt{\left(\sum_{i=1}^{N} f^2(\vec{x}_i) \right) - \left(\sum_{i=1}^{N} f(\vec{x}_i) \right)^2} \ . \tag{C.4}$$

The Monte Carlo integration is implemented in the program using [23].

References

[1] M. Janoschek, *et al.* "Fluctuation-induced first-order phase transition in Dzyaloshinskii-Moriya helimagnets." Phys. Rev. B **87**, 134407 (2013).

[2] A. Bauer, M. Garst, and C. Pfleiderer. "Specific Heat of the Skyrmion Lattice Phase and Field-Induced Tricritical Point in MnSi." Phys. Rev. Lett. **110**, 177207 (2013).

[3] J. Kindervater, *et al.* "Critical spin-flip scattering at the helimagnetic transition of MnSi." Phys. Rev. B **89**, 180408(R) (2014).

[4] I. Stasinopoulos (2015). Unpublsihed results.

[5] S. Mühlbauer, *et al.* "Skyrmion Lattice in a Chiral Magnet." Science **323**, 915 (2009).

[6] I. E. Dzyaloshinskii. "A Thermodynamic theory of weak ferromagnetism of antiferromagnets." J. Phys. Chem. Sol. **4**, 241 (1958).

[7] T. Moriya. "Anisotropic Superexchange Interaction and Weak Ferromagnetism." Phys. Rev. **120**, 91 (1960).

[8] M. Garst (2014/15). Private communication.

[9] T. H. R. Skyrme. "A Non-Linear Field Theory." Proc. R. Soc. A **260**, 127 (1961).

[10] S. M. H. Wong. "What exactly is a Skyrmion?" arXiv: hep-ph/0202250v2 (2002).

[11] K. Everschor. *Current-Induced Dynamics of Chiral Magnetic Structures.* Ph.D. thesis, University of Cologne (2012).

[12] T. Schwarze, *et al.* "Universal helimagnon and skyrmion excitations in metallic, semiconducting and insulating chiral magnets." Nature Materials **14**, 478–483 (2015).

[13] T. Adams, *et al.* "Long-Range Crystalline Nature of the Skyrmion Lattice in MnSi." Phys. Rev. Lett. **107**, 217206 (2011).

[14] S. V. Grigoriev, *et al.* "Interplay between crystalline chirality and magnetic structure in $Mn_{1-x}Fe_xSi$." Phys. Rev. B **81**, 012408 (2010).

[15] S. A. Brazovskii, I. E. Dzyaloshinskii, and A. Muratov. "Theory of weak crystallization." Zh. Eksp. Teor. Fiz. **93**, 1110–1 124 (1987).

[16] S. A. Brazovskii. "Phase transition of an isotropic system to a nonuniform state." Sov. Phys.-JETP **41**, 1 (1975).

[17] J. Cornwall, R. Jackiw, and E. Tomboulis. "Effective action for composite operators." Phys. Rev. D **10**, 2428 (1974).

[18] M. Garst. "Quantum Many Body Theory." Lecture notes. Unpublished.

[19] A. Bauer, *et al.* "Quantum phase transitions in single-crytal $Mn_{1-x}Fe_xSi$ and

$Mn_{1-x}Co_xSi$: Crystal growth, magnetization, ac susceptibility, and specific heat." Phys. Rev. B **82**, 064404 (2010).

[20] J. Kindervater (2014/15). Unpublished results.

[21] G. Baym and G. Grinstein. "Phase transition in the σ model at finite temperature." Phys. Rev. D **15**, 2897 (1977).

[22] A. Altland and B. Simons. *Condensed Matter Field Theory.* 2nd edition (Cambridge University Press, Cambridge, 2010).

[23] M. Galassi. *GNU Scientific Library Reference Manual.* ISBN 0954612078, 3rd edition.

[24] N. Metropolis, *et al.* "Equation of State Calculations by Fast Computing Machines." J. Chem. Phys **21**, 1087 (1953).

List of Figures

Danksagung

Zu allererst bedanke ich mich ganz herzlich bei meinen beiden Betreuern PD Markus Garst und Prof. Achim Rosch.

Ich danke Prof. Achim Rosch, dass er es mir ermöglicht hat, diese Arbeit bei ihm und Markus Garst zu schreiben. Vielen Dank für die Anleitungen und Tipps, beispielsweise wie man Fehler findet und eigene Rechnungen sinnvoll überprüft. Ich danke ihm, dass ich so viel von ihm lernen durfte und hoffe, dass ich auch in Zukunft an interessanten und mit physikalischen Einsichten gefüllten Diskussionen mit ihm teilhaben darf.

Ganz herzlich bedanke ich mich bei PD Markus Garst. Es macht mir immer großen Spaß, mit ihm zusammenzuarbeiten. Ich danke ihm für die wirklich großartige Betreuung - er hat mich an die Hand genommen und mir bei den ersten eigenen Schritten geholfen. Insbesondere danke ich ihm für seine unglaubliche Geduld, für die vielen Erklärungen und für die Aufmunterungen und Hilfestellungen, wenn Rechnungen mal nicht so geklappt haben. Ich freue mich schon sehr auf die Zusammenarbeit in den kommenden Jahren.

Ich möchte außerdem den "Doktoranden meines Vertrauens", Robert Bamler, Maximilian Genske und Sarah Schroeter dafür danken, dass sie sich immer Zeit genommen haben, um mit mir spontan Fragen zu diskutieren. Das Zusammensein mit ihnen im Büro hat den Alltag immer noch erfreulicher gemacht. Ich danke Robert Bamler für seine Hilfe bei der Monte-Carlo-Integration.

Rosa-Belle Gerst und Johannes Waizner gilt mein Dank für das Korrekturlesen und hilfreiche Hinweise. Stephanie Matern verdanke ich viele erholsame und manchmal mit hilfreichen Diskussionen gefüllte Kaffeepausen. Liebe Steffi, ich werde dich vermissen.

Zu guter Letzt möchte ich mich bei der Bonn-Cologne Graduate School of Physics and Astronomy für die Förderung und finanzielle Unterstützung bedanken.

Eigenständigkeitserklärung

Hiermit erkläre ich, dass ich diese Arbeit selbständig verfasst habe. Alle verwendeten Quellen und Hilfsmittel sind angegeben.

Köln, den 10.11.2015

Laura Köhler